PAPER

Check for updates

Evaluation of Cu- and Mn-doped Co$_3$O$_4$/NiO composites as cathodes for intermediate temperature solid oxide fuel cells

Syed Ansar Ali Shah,[a] Amir Sultan,[bc] Kun Zheng, [iD][cd] Muhammad Tariq Sajjad [iD][e] and Richard T. Baker [iD] *[a]

This work advances Co$_3$O$_4$–NiO-based composite cathodes for intermediate-temperature solid oxide fuel cells (IT-SOFCs). In this study, we investigate the potential benefits of combining two electronically conducting phases in a composite system (Co$_3$O$_4$/NiO) and of doping this with Mn and Cu. The undoped, Mn-doped, and Mn/Cu-doped composites were synthesised and subjected to comprehensive structural, morphological, and electrochemical characterisation. X-ray diffraction confirmed phase purity, with Mn preferentially incorporating into the Co$_3$O$_4$ lattice, reducing crystallite size and enhancing surface area. Electron microscopy revealed that Mn doping suppressed particle agglomeration, promoting uniform porosity, while dynamic light scattering confirmed the presence of nanoparticles in this composition. Electrochemical impedance spectroscopy demonstrated superior catalytic performance for the Mn-doped composite, with distribution of relaxation time (DRT) analysis indicating accelerated oxygen reduction kinetics. Humidification of the cathode gas slightly increased polarization resistance, which is consistent with electronic conduction being dominant. Thermal stability tests confirmed chemical compatibility with GDC and YSZ electrolytes during annealing at 800 °C for 100 h. The Mn-doped composite emerged as the best candidate, balancing microstructural properties, rapid charge-transfer dynamics, and thermal stability, positioning it as a competitive cathode material for energy-efficient SOFCs.

1. Introduction

According to the International Energy Agency, global demand for energy is expected to increase by 50% by the year 2050, with most of this growth expected to occur in developing countries.[1,2] At the same time, the sustainability of our energy systems is also greatly challenged by air pollution, climate change, and other environmental issues. In response to these challenges, there is an urgent need for innovative technologies that can provide clean, efficient, and reliable energy while reducing emission of greenhouse gases and other environmental pollutants.[2] One of the most promising technologies in this domain is the solid oxide fuel cell (SOFC).

SOFCs represent a very attractive technology for electrical power generation because of their relatively high overall efficiencies and very low environmental impact. SOFC systems produce no, or low CO$_2$ emissions (depending on fuel used), generate little noise pollution, possess flexibility in terms of fuel choice, and have been demonstrated to operate over long lifetimes, up to 80 000 h.[3,4] A SOFC employs a dense solid oxygen ion-conducting electrolyte (typically yttrium-stabilized zirconia, YSZ). At the cathode of the SOFC, oxygen molecules are adsorbed from an oxidant stream (usually air) and are reduced electrochemically to form O^{2-} ions using electrons taken from the external circuit (the Oxygen Reduction Reaction, ORR). These ions then pass through the electrolyte (due to the chemical potential gradient) to the anode, which is exposed to the fuel stream. These oxygen ions oxidize the fuel electrochemically, generating electrons that enter the external circuit. An electronic current is thus generated in any load included to the external circuit.[4]

SOFC researchers are currently working to develop more active electrode materials in order to decrease the operating temperature of SOFCs,[5] allow them to be used more efficiently, and with reduced carbon dioxide emissions.[6] For cathodes to be employed at intermediate and lower temperatures, it is crucial

[a]EaStChem School of Chemistry, University of St Andrews, St Andrews, Fife, KY16 9ST, UK. E-mail: rtb5@st-andrews.ac.uk; Tel: +44-1334 463899

[b]Jerzy Haber Institute of Catalysis and Surface Chemistry, Polish Academy of Sciences, Niezapominajek 8, 30-239 Krakow, Poland

[c]Faculty of Energy and Fuels, AGH University of Krakow, Al. A. Mickiewicza 30, 30-059 Krakow, Poland

[d]AGH Centre of Energy, AGH University of Krakow, Ul. Czarnowiejska 36, Krakow, 30-054, Poland

[e]Division of Electrical and Electronic Engineering, |School of Engineering, London South Bank University, London SE1 0AA, UK

that the cathodic polarisation resistances have acceptably low values.[7]

To improve the performance and compatibility of cathode materials, specifically in terms of the polarisation resistance and the thermal expansion coefficient, various strategies have been employed. These include nano-structuring,[8–14] doping[15–20] and composite formation.[7,21–23] Composite formation in cathode materials is mainly targeted at enhancing the oxygen diffusion properties of the material by introducing an amount of the ionically conducting electrolyte (which can also improve thermal expansion compatibility with the electrolyte),[7] or to enhance the ORR activity of a cathode material by the introduction of other materials/phases (forming heterointerfaces) possessing enhanced catalytic properties.[24]

The use of Co_3O_4 to improve ORR performance has been reported in several studies.[25–27] Because of its good catalytic and electrochemical properties, it is employed in applications such as batteries,[28,29] supercapacitors,[30,31] and SOFCs.[32] Rehman and coworkers used a composite of Co_3O_4/GDC (Gd doped ceria) as a cathode for intermediate temperature SOFCs and reported polarisation resistances in the range, $0.69–0.92 \ \Omega \ cm^{-2}$, at 800 °C during the first 200 h of operation.[32] Similarly, Yang and coworkers added Co_3O_4 to BSCF ($Ba_{0.5}Sr_{0.5}Co_{0.8}Fe_{0.2}O_{3-\delta}$) in a proton-conducting SOFC using BCZY ($BaCe_{0.7}Zr_{0.1}Y_{0.2}O_{3-\delta}$) as the electrolyte. Compared to the bare BSCF cathode, the BCZY/Co_3O_4 composite not only improved catalytic activity but also showed better adhesion to the surface of the electrolyte.[33] Chen and coworkers introduced Co_3O_4 in their LSCF ($La_{0.6}Sr_{0.4}Co_{0.2}Fe_{0.8}O_{3-\delta}$) electrode used with an 8 mol% YSZ electrolyte and found that the cathodic polarisation of the LSCF/Co_3O_4 was markedly lower, and electrode–electrolyte adhesion better, compared to the bare LSCF.[34] Several other studies also conclude that the introduction of Co_3O_4 causes the cathodic polarisation resistance to decrease the catalytic activity and the overall performance of the cell to be remarkably enhanced.[35–38]

NiO is a p-type semiconductor which has also been introduced as a secondary phase to improve the ORR and decrease the polarisation resistance of SOFC cathode materials.[39–43] Yang and coworkers decorated the surface of their $SrFe_{0.85}Ti_{0.1}Ni_{0.05}O_{3-\delta}$ electrode with NiO, which showed superior ORR activity and decreased polarisation resistance compared to the bare electrode.[39] Liang and coworkers synthesised cathode material with the overall composition, $Ba_{0.95}(Co_{0.4}Fe_{0.4}Zr_{0.1}Y_{0.1})_{0.95}Ni_{0.05}O_{3-\delta}$ which includes a NiO phase. Their analysis concluded that this material showed superior ORR activity compared to the Ni-free $BaCo_{0.4}Fe_{0.4}Zr_{0.1}Y_{0.1}O_{3-\delta}$.[40] Yao and coworkers found that introducing the NiO phase in $PrBaFe_{1.9}Mo_{0.1}O_{6-\delta}$ reduced cathode polarisation resistance and activation energy, hence giving faster ORR kinetics.[41] Lee and coworkers synthesised $BaCo_{0.4}Fe_{0.4}Zr_{0.1}Y_{0.1}O_{3-\delta}$ (BCFZY) cathode material for protonic ceramic fuel cells (PCFCs). Even though it is an impressive ionic and electronic conductor itself, they found that the addition of NiO resulted in reduced polarisation resistance and enhanced performance of the cell.[42] Nadeem and coworkers calculated the effective oxygen chemical surface exchange coefficient for bare LSCF and NiO/LSCF composite cathodes and found that at 800 °C, the value

for the composite was almost double that of the bare LSCF. They also reported a reduction in the polarisation resistance of their electrode material and enhancement of the overall performance of the cell with NiO addition.[43]

Owing to these properties as reported in the literature, composites of NiO and Co_3O_4 are expected to have superior electrochemical performance and to be appealing candidates for electrochemical applications. For instance, Jiang and co-workers synthesised NiO/Co_3O_4 as an electrode material for supercapacitors and concluded that the electrochemical performance of the composite was much superior to the performance of NiO and Co_3O_4 individually.[44] Several other studies also show that incorporation of NiO/Co_3O_4 composites gives rise to enhanced electrochemical performance.[45–51] Wang and co-workers synthesised and evaluated LSM ($La_{0.8}Sr_{0.2}MnO_3$) electrodes in solid electrolyte cells and found that the incorporation of both NiO and Co_3O_4 in the electrode decreased its specific polarisation resistance as well as enhancing the efficiency of NO_x removal.[52] Nayak and co-workers synthesised NiO/Co_3O_4 composites in different ratios and evaluated their electrochemical performance in terms of the ORR. They found that NiO : Co_3O_4 in the ratio of 1 : 2 showed excellent electrochemical performance (as electrocatalysts for ORR) compared to the other proportions.[53] Wang and co-workers compared the performance of undoped and Mn-doped Co_3O_4 for application as electrodes) in supercapacitors and found that addition of Mn introduced oxygen defects in the structure which resulted in improved electrochemical performance.[54] Behera and co-workers found that Cu doping in Co_3O_4 enhanced its electrochemical bifunctionality (ORR and OER) for application in Zinc–air batteries.[55] Similarly, Yuan and co-workers found improvement in the electrochemical performance of NiO with Cu doping for application in supercapacitors.[56]

Given the significance of NiO/Co_3O_4 composites in energy applications and the critical role of dopants in modulating their properties, this study focuses on synthesising NiO/Co_3O_4 composites alongside their Mn-doped and Mn/Cu co-doped variants. In this study, we investigate the potential benefits of combining two electronically conducting phases in a composite system (Co_3O_4/NiO) and of doping this with Mn and Cu. A systematic structural analysis was conducted to evaluate phase homogeneity and confirm the successful integration of dopants within the biphase matrix. These materials were subsequently investigated as potential cathode candidates for SOFCs, and their performance related to their compositional uniformity and dopant distribution.

2.   Experimental

2.1.   Materials synthesis

The nanocomposites were fabricated employing a citric acid-based sol–gel method.[57] Precise stoichiometric quantities of the nitrate precursors, $Al(NO_3)_3 \cdot 6H_2O$ (Sigma-Aldrich, ≥98%), $Co(NO_3)_2 \cdot 6H_2O$ (Acros ThermoFisher Scientific, 98%), $Ni(NO_3)_2 \cdot 6H_2O$ (Fluka, ≥97%) and $Mn(NO_3)_2 \cdot 4H_2O$ (Acros ThermoFisher Scientific, ≥98%), corresponding to the molar ratios outlined in Table 1 and sufficient to prepare 0.033 moles

This journal is © The Royal Society of Chemistry 2025

J. Mater. Chem. A, 2025, **13**, 29486–29503 | **29487**

Table 1 Molar ratios of the precursors used to synthesise the undoped and doped composites studied

Sample	Co	Ni	Mn	Cu
NiO/Co_3O_4	2	1	0	0
Mn-doped NiO/Co_3O_4	2	0.85	0.15	0
Mn/Cu doped NiO/Co_3O_4	2	0.85	0.075	0.075

of total oxides, were dissolved in 200 mL of deionized water and homogenized under continuous stirring for 30 min. Citric acid, with Co : Ni : citric acid molar ratio = 2 : 1 : 4, was added, and the solution was heated to 80 °C for 1 h. The temperature was then raised to 110 °C until the formation of a viscous gel, which was dried at 140 °C for 1 h in a box furnace. The resulting xerogel was calcined at 800 °C in static air in a tube furnace.

Three distinct materials were synthesised: (a) undoped Co_3O_4/NiO composite, prepared with a Co : Ni molar ratio of 2 : 1; (b) Mn-doped Co_3O_4/NiO: in which the Co ratio of the undoped sample was modified by substituting 15% of Ni by Mn; (c) Mn/Cu co-doped Co_3O_4/NiO, in which equal molar amounts of Mn and Cu dopants (7.5% each) were to be incorporated in the composite. These details are summarised in Table 1.

2.2. Materials characterisation

The phase composition and crystallographic parameters of the materials synthesised were analysed *via* powder X-ray diffraction (XRD) using a Panalytical X'Pert diffractometer with Cu Kα radiation ($\lambda = 1.5405$ Å). Scans were performed across a 2θ range of 10–90° at an angular increment of 0.008° under operating conditions of 40 kV and 30 mA. Phase quantification was carried out using *.cif files from the ICSD database, and fitting was carried out using the Rietveld refinement function using the Panalytical software, Highscore Plus. Fourier-transform infrared (FTIR) spectra were recorded at 400–3500 cm^{-1} using a Shimadzu IRAffinity 1S spectrometer.

The morphology and cross-section of the symmetrical electrochemical cells were studied by obtaining high resolution Scanning Electron Microscopy (SEM) images employing MIRA3-TESCAN and JEOL JSM-7500 F instruments.

Quantitative particle size distribution profiles were obtained using dynamic light scattering (DLS) measurements conducted on a Malvern Panalytical Mastersizer 3000 system, with volumetric percentage distributions calculated in order to resolve polydispersity and dominant particle size fractions.

Microstructural and elemental distribution studies were conducted *via* Transmission Electron Microscopy (TEM) on a Titan Themis S/TEM system (200 keV, FEI), incorporating a spherical aberration corrector and an X-FEG Schottky emitter. Elemental mapping and semi-quantitative composition analysis were achieved using the integrated Super-X energy-dispersive X-ray spectroscopy (EDS) detector. Specimens for TEM were prepared by ultrasonically dispersing powdered samples in acetone, followed by deposition onto holey carbon-coated copper grids (for samples with no Cu) and carbon-coated gold grids (for samples containing Cu).

Specific surface area and pore size distributions were obtained *via* nitrogen adsorption–desorption isotherms using a Micromeritics Tristar II instrument, with Brunauer–Emmett–Teller (BET) and Barrett–Joyner–Halenda (BJH) models applied to derive surface area and mesopore characteristics, respectively. Prior to analysis, samples were subjected to degassing at 150 °C for 12 h under vacuum.

Chemical state analysis was performed by X-ray photoelectron spectroscopy (XPS) using a Kratos Axis Ultra DLD spectrometer equipped with a monochromatic Al Kα source (1486.6 eV, 15 kV, 4 mA). High-resolution spectra for Co 1s, Ni 2p, Mn 2p, Cu 2p, and O 1 s regions were acquired under ultrahigh vacuum ($\sim 1 \times 10^{-10}$ mbar). Spectral deconvolution and peak fitting were conducted using CasaXPS software (v2.3.25), ensuring accurate identification of local chemical environments.

To evaluate the chemical compatibility and thermal stability of the synthesized Mn-doped Co_3O_4/NiO composite for SOFC applications, equal mass mixtures of the composite with gadolinium-doped ceria (GDC) and yttria-stabilized zirconia (YSZ) electrolyte powders were hand-milled and subjected to thermal treatment at 800 °C for 100 h. Post-annealing XRD patterns were then compared with those for fresh electrolyte and cathode materials.

2.3. Cell fabrication and electrochemical evaluation

Gd-doped ceria (GDC) pellets were utilized as the electrolyte for electrochemical impedance spectroscopy (EIS) measurements. The GDC powder (fuel cell materials) was pressed into pellets using a hydrostatic pressure of 400 MPa for approximately 1 min. These pellets were sintered at 1425 °C for 5 h in air. The diameter and thickness of the resulting electrolyte disks were 13 mm and 0.5 mm, respectively. The synthesised composite cathode powders were formulated into pastes and screen-printed in a circular pattern on both sides of the GDC pellets to create symmetrical electrode–electrolyte-electrode configurations using an Aremco 3230 screen printer. The pastes were optimised by thorough mixing with an ink vehicle to achieve the desired rheological characteristics. After three successive depositions on each side, the electrodes were dried in an oven at 90 °C for 15 min, after which the cells were sintered in air at 800 °C for 2 h, employing heating and cooling rates of 3 °C min^{-1}.

To make current collectors, silver paste (from fuel cell materials) was applied in a mesh configuration on both electrode surfaces using an appropriate brush and heated at 750 °C for 30 min with heating and cooling rates of 3 °C min^{-1}. These symmetrical cells were subsequently assessed to determine the electrode polarisation resistance over a temperature range of 550–800 °C in both dry and 3 vol% H_2O-enriched air atmospheres.

Electrochemical performance was characterised by Electrochemical Impedance Spectroscopy (EIS) using a Solartron 1252A frequency response analyser in conjunction with a Solartron SI 1287 electrochemical interface. Impedance spectra were obtained under open-circuit conditions within a frequency range

29488 | *J. Mater. Chem. A*, 2025, **13**, 29486–29503

This journal is © The Royal Society of Chemistry 2025

of 0.1 Hz to 1 MHz, using a perturbation amplitude of 25 mV. EIS spectra were recorded on the symmetrical cells prepared as above with GDC electrolytes and using each of the three composite materials in turn to form both electrodes. Either dry air or humidified air (3% water) was supplied to both electrodes and spectra were obtained at operating temperatures between 650 and 800 °C. The overall interfacial polarisation and ohmic resistance (R_Ω) were modelled. This was based on a L-R_Ω-(-RQ)$_{HF}$–(RQ)$_{LF}$ equivalent circuit, where Q represents a capacitive constant phase element, R denotes resistance, L is inductance, and the subscripts HF and LF correspond to the high- and low-frequency components, respectively. The EIS data were fitted using Z-View software (from Solartron) and were further analysed in MATLAB to obtain Distribution of Relaxation Time (DRT) plots in order to study the physicochemical processes occurring in the symmetrical cells in detail.

A long-term EIS study of the Mn-doped Co_3O_4–NiO cathode material deposited on a GDC electrolyte was conducted for a period of 100 h in air at 800 °C. A symmetrical cell with the configuration, Mn-doped Co_3O_4–NiO|GDC|Mn-doped Co_3O_4–NiO, was prepared by depositing the Mn-doped Co_3O_4–NiO paste (mixed with an ink vehicle) by screen-printing (Aremco 3230) it three times on each side of the GDC pellet, with a drying treatment at 90 °C for 15 min in an oven after each application. After deposition of the electrode layers, the cell was heated in a furnace for 2 h at 800 °C. For the current collectors, silver paste was deposited in the form of a mesh on both faces and the cell again heated in a furnace for 30 min at 750 °C.

3. Results and discussion

3.1. X-ray diffraction

X-Ray diffractograms of the synthesised composites are shown in Fig. 1, and are compared with ICSD reference patterns for the individual oxides, Co_3O_4 and NiO (36256 [58] and 9866,[59] respectively). All the diffractograms confirmed the presence of both phases. Co_3O_4 and NiO crystallise in cubic $Fd\bar{3}m$ and cubic $Fm\bar{3}m$ phases, respectively. Doping with Mn and Cu did not introduce any impurity phases in the composites, confirming the successful incorporation of the dopants into the host phases. Phase quantification, using Rietveld refinement, and the average crystallite sizes, calculated from the prominent peaks using Scherrer's equation[60] for both oxide phases, are summarised in Table 2. The strong decrease in the crystallite size of the Co_3O_4 phase and the increase in its quantification (%) with Mn doping indicate that Mn is more favourably incorporated in the Co_3O_4 phase (also confirmed in EDS mapping – see below). A strong decrease in the crystallite size of Co_3O_4 with Mn-doping has been reported previously.[61]

3.2. Fourier transform infrared spectroscopy

Fig. 2 shows the FTIR spectra obtained for the synthesised composites. The peaks in the region, 550–600 cm^{-1} and 620–690 cm^{-1}, correspond to the bending vibration modes of Co(II)–O and Co(III)–O, respectively. Hence, the presence of both Co^{3+} and Co^{2+} supports the presence of spinel-structured Co_3O_4. The
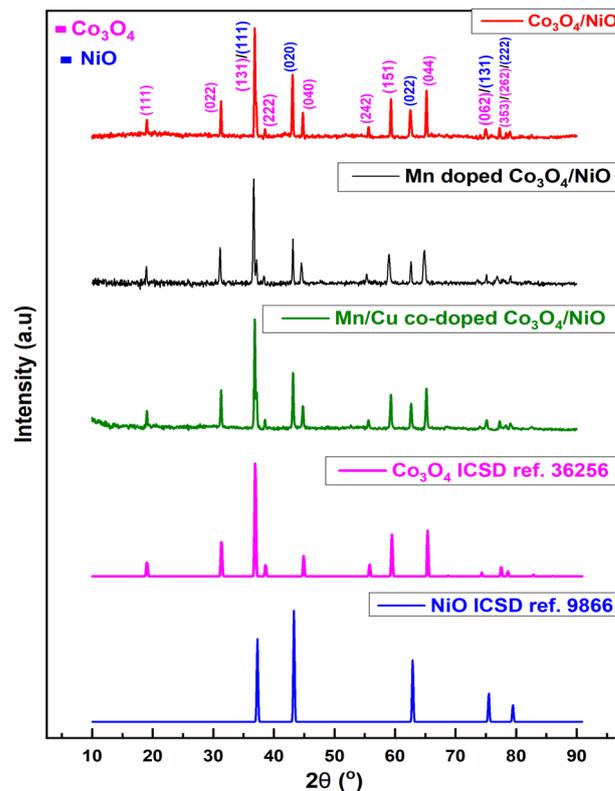

Fig. 1 X-ray diffractograms of the synthesised composites together with reference patterns for Co_3O_4 and NiO from the ICSD.

band in the range 450–550 cm^{-1} confirms the presence of Ni–O.[62] The stretching vibration of Ni–O at 663 cm^{-1} is also reported in the literature,[63] but here this overlaps with, and is obscured by, the bending mode of Co(III)–O.

3.3. Nitrogen physisorption and dynamic light scattering

Fig. 3(a) presents the N_2 physisorption isotherms, which present the amount of N_2 adsorbed on the surface of the nanocomposites as a function of both increasing and decreasing applied relative pressure, from 0 to 1 (representing atmospheric pressure). All of the materials gave a type-III isotherm, which is obtained when the adsorbent–adsorbate interaction is weak. The Mn-doped Co_3O_4/NiO material shows the highest values for N_2 adsorption. Fig. 3(b) shows the pore size distribution for the composites. All composites show two main peaks: one in the region, 17–40 nm, which indicates that

Table 2 Phase quantification and crystallite size estimates for the synthesised composites

Composite	Quantification (%)		Crystallite size (nm)	
	Co_3O_4	NiO	Co_3O_4	NiO
Co_3O_4–NiO	65.3	34.7	44.9	36.7
Mn-doped Co_3O_4–NiO	75.8	24.2	28.9	42.6
Mn/Cu-doped Co_3O_4–NiO	69.0	31.0	37.2	38.4

This journal is © The Royal Society of Chemistry 2025

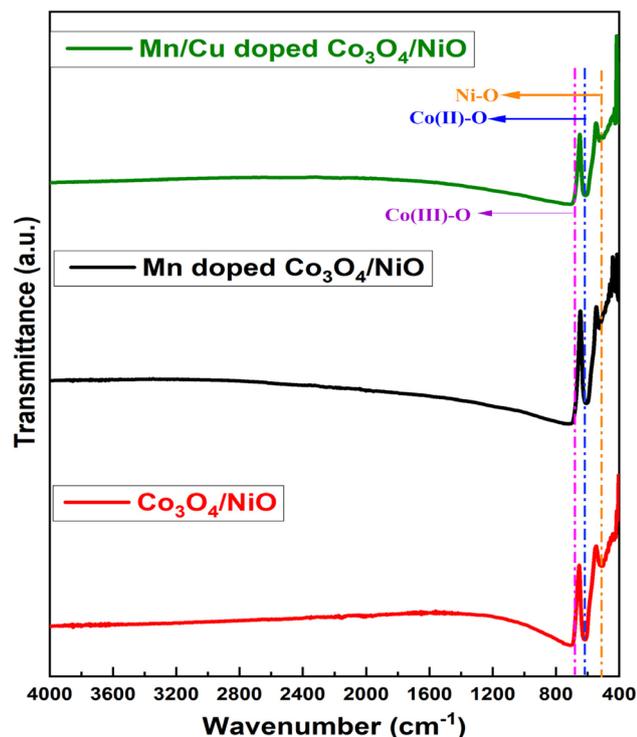*J. Mater. Chem. A*, 2025, **13**, 29486–29503 | **29489**

Fig. 2 FTIR spectra of the synthesised nanocomposites.

the materials are mesoporous, and the second peak, at 96–128 nm, which most likely corresponds to interparticle voids. The BET surface area, pore width, and pore volume obtained by

BET and BJH analysis of these data are listed in Table 3. The pore widths relate to the mesopore range only and are consistent with the peaks seen in Fig. 3(b) at around 25 nm.

Fig. 4 presents particle size distribution plots for all three composites obtained using the dynamic light scattering technique. The Mn-doped composite has an extra peak in the lower particle size region, which shows that a large volume fraction relates to particles in the range 10–287 nm (with its peak maximum at 38 nm). This reduction in particle size could be due to the reduction in the crystallite size of the Co_3O_4 phase, resulting in finer particles. A reduction in the particle size of Co_3O_4 on doping with Mn has been reported previously.[61]

3.4. Transmission electron microscopy and energy dispersive spectroscopy

Figures 5–7 present analyses obtained using the S/TEM microscope with Energy Dispersive Spectroscopy (EDS) detector of the three composite samples in turn. Electron images obtained in High-Angle Annular Dark-Field (HAADF) mode show the density distribution across particles of each sample. EDS maps and corresponding line-scans show the variation of the relevant elements as a function of position. EDS spectra of relatively large areas of each sample are also included to give general compositional information.

Fig. 5 shows the HAADF image of particles of the Co_3O_4/NiO sample (Fig. 5(a)) together with corresponding elemental maps of the individual constituent elements, Co, Ni, and O (Fig. 5(b–d)), and of Co and Ni together (Fig. 5(e)). It is obvious from these maps that Co and Ni form separate phases rather than any
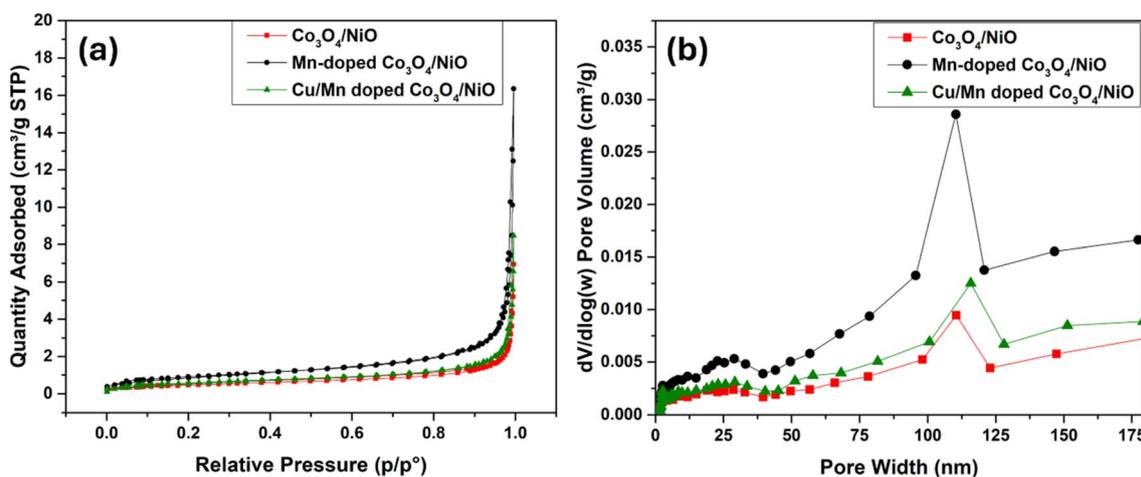

Fig. 3 (a) N_2 physisorption isotherms and (b) pore size distributions for the synthesised nanocomposites.

Table 3 BET surface area, pore width and pore volume of the synthesised composites

Sample	BET surface area ($m^2 g^{-1}$)	Pore width (nm)		Pore volume ($\times 10^{-3}$, $cm^3 g^{-1}$)	
		Adsorption	Desorption	Adsorption	Desorption
Co_3O_4/NiO	1.66	15.8	22.0	6.83	10.9
Mn doped Co_3O_4/NiO	3.20	27.9	31.0	19.3	25.2
Mn/Cu doped Co_3O_4/NiO	2.07	18.9	27.2	8.65	12.9

29490 | *J. Mater. Chem. A*, 2025, **13**, 29486–29503
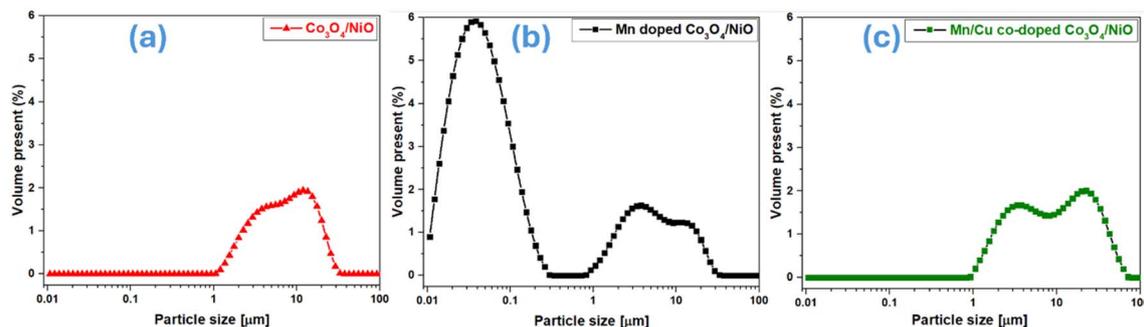
This journal is © The Royal Society of Chemistry 2025

Fig. 4 Particle size distributions obtained with the dynamic light scattering technique for (a) Co_3O_4/NiO, (b) Mn-doped Co_3O_4/NiO, and (c) Mn/Cu-doped Co_3O_4/NiO.

mixed phase. The EDS maps also confirm excellent distribution and mixing of these two phases, and good interconnection between the particles of each phase. The EDS spectrum (Fig. 5(f)) confirms the presence of Co and Ni in the ratio expected, and the absence of impurities. The Cu and C detected originate from the Cu/C TEM grid used to support these samples.

In the HAADF image and corresponding EDS maps for the Mn-doped Co_3O_4/NiO material, it is obvious again that the Co and Ni are present in completely separate phases, and that the nanoparticles of these two phases are well distributed and mixed (Fig. 6(e)). Importantly, the Mn (Fig. 6(f)) shows the same spatial distribution as Co. The fact that Mn and Co are coincident implies the selective doping of Mn into the Co_3O_4, rather than the NiO phase. This is consistent with the discussion of the XRD results above (Section 3.1), and is further demonstrated in the combined maps of Co and Mn and of Ni and Mn in Fig. 6(g) and (h), respectively. Fig. 6(i) shows the variation in elemental composition along the arrow drawn in Fig. 6(e) to show the

mixing of Co, Ni and Mn. This plot shows the sharp changes between the Co and Ni-containing phases. It also shows that the Mn exactly follows the trend in Co and opposes the trend in Ni, which again implies the incorporation of Mn in the Co_3O_4 phase over the NiO phase. The EDS spectrum in Fig. 6(j) shows the presence of all the constituent elements of Mn-doped Co_3O_4/NiO (with Cu and C originating again from the TEM grid).

Fig. 7 presents the HAADF image and corresponding EDS maps for the Mn/Cu-doped Co_3O_4/NiO sample. It can be seen that Mn behaves in the same way as in the Mn-doped composite and is incorporated exclusively into the Co_3O_4 phase. However, the Cu is incorporated into both the Co_3O_4 and NiO host phases, which is clear from the maps of the individual elements as well as in the combined map of Mn, Ni and Cu together (Fig. 7(h)). Fig. 7(i) shows a higher magnification EDS map and an EDS line scan obtained from the area selected on this map (shown in Fig. 7(j)) which shows that Mn is again following the same trend as Co, but that Cu is present in both host phases.
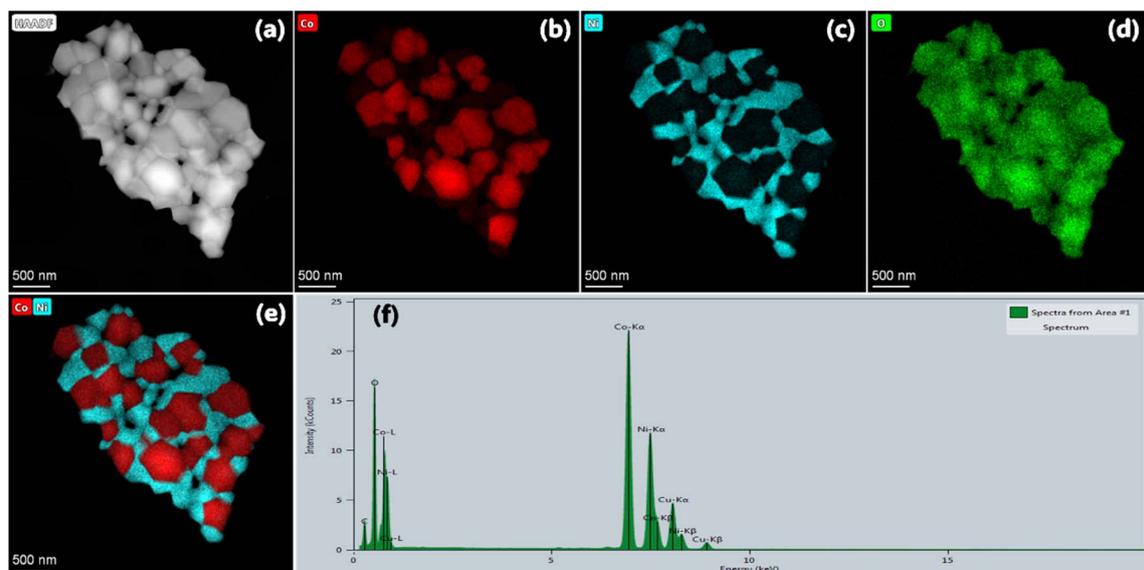

Fig. 5 Co_3O_4/NiO sample: (a) HAADF electron image; (b–e) EDS elemental distribution maps for Co, Ni, and O, and Ni and Co combined, respectively; (f) general EDS spectrum of the Co_3O_4/NiO heterostructure.
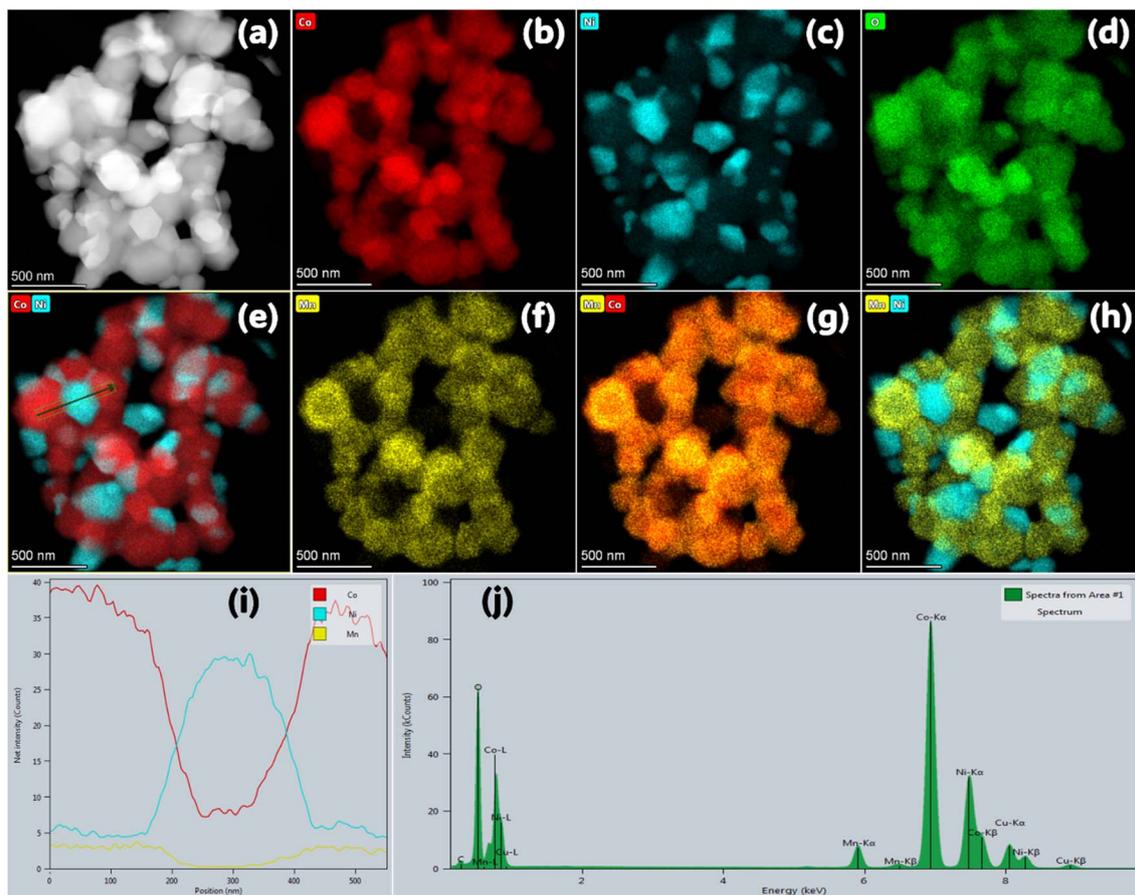
Fig. 6 Mn-doped Co_3O_4/NiO sample: (a) HAADF electron image; (b–e) EDS elemental distribution maps for Co, Ni, and O, and Co and Ni combined, respectively; (f–h) EDS maps for Mn, Mn and Co, and Mn and Ni, respectively; (i) EDS line scan along the arrow drawn in panel e; and (j) EDS spectrum of Mn-doped Co_3O_4/NiO nanocomposite.

Fig. 7(k) presents the EDS spectrum of a relatively large area of the sample and confirms the presence of the constituent elements (since the sample contains Cu, an Au/C TEM grid was used, giving an EDS peak for Au).

3.5. X-ray photoelectron spectroscopy

Fig. 8(a) presents XPS analysis of all three composite samples in wide, survey scans and in high resolution scans in Co 2p, Ni 2p, Mn 2p, Cu 2p, and O 1s regions. For Co 2p in Fig. 8(b), the peaks in the regions 779.2–781.4 eV and 794.3–796.9 eV correspond to Co $2p_{1/2}$ and $2p_{3/2}$, respectively. The deconvoluted peaks assigned to Co^{3+} and Co^{2+} are positioned at 779–780.3 eV and 781–782 eV, respectively.[64] There is a shift to lower binding energy of the Co peak on going from the undoped to both of the doped composites, indicating a shift from Co^{2+} (tetrahedral sites) to Co^{3+} (octahedral).[65] The Ni 2p spectra in Fig. 8(c) show four distinct peaks: the peaks at 850–869 eV and 870–885 eV correspond to Ni $2p_{3/2}$ and $2p_{1/2}$, respectively. The deconvoluted peak corresponding to Ni^{2+} and Ni^{3+} occurs at BE values of 854.8–855.5 eV and 855.5–856.5 eV, respectively.[66] The XPS peak for Mn (Fig. 8(d)) in the Mn-doped and Mn/Cu-doped samples is observed at 642.6 eV and corresponds to Mn^{3+}.[65] The Mn peaks overlap with the Ni Auger LMM relaxations[67] which are seen in

all the samples including the undoped composite. Fig. 8(e) shows the XPS spectra for Cu 2p. The peaks at 934.3 eV and 954.2 correspond to Cu $2p_{3/2}$ and $2p_{1/2}$, respectively (S1 and S2 are satellite peaks corresponding to Cu $2p_{3/2}$ and $2p_{1/2}$, respectively).[68] Table 4 contains the atomic ratios corresponding to the Ni^{3+}/Ni^{2+} and Co^{3+}/Co^{2+} oxidation states calculated from the areas of the respective deconvoluted peaks. With Mn doping, these results show a marked shift from Co^{2+} (in tetrahedral spinel sites) to Co^{3+} (octahedral) in the Co_3O_4 in the Mn-doped material. This is related to the incorporation of Mn^{3+}. The Ni in the NiO phase also gains electron charge. This is consistent with charge migrating from Co_3O_4 to NiO (Co sites are oxidised and Ni sites reduced). Conversely, co-doping with Cu and Mn reverses this trend (i.e., Ni loses electron charge while Co gains electron charge). These opposing trends with Mn and Mn/Cu doping suggest some charge exchange between the two phases of the composite materials (when dopants are incorporated into their crystal structures). The slight shifting of the cation features (for Co 2p and Ni 2p in this case) towards lower BE on Mn and Cu doping also suggests an increase in the local electron density due to the formation of oxygen vacancies.[69,70] Such vacancies would be expected to contribute to the enhancement of electrochemical performance, specifically related to the
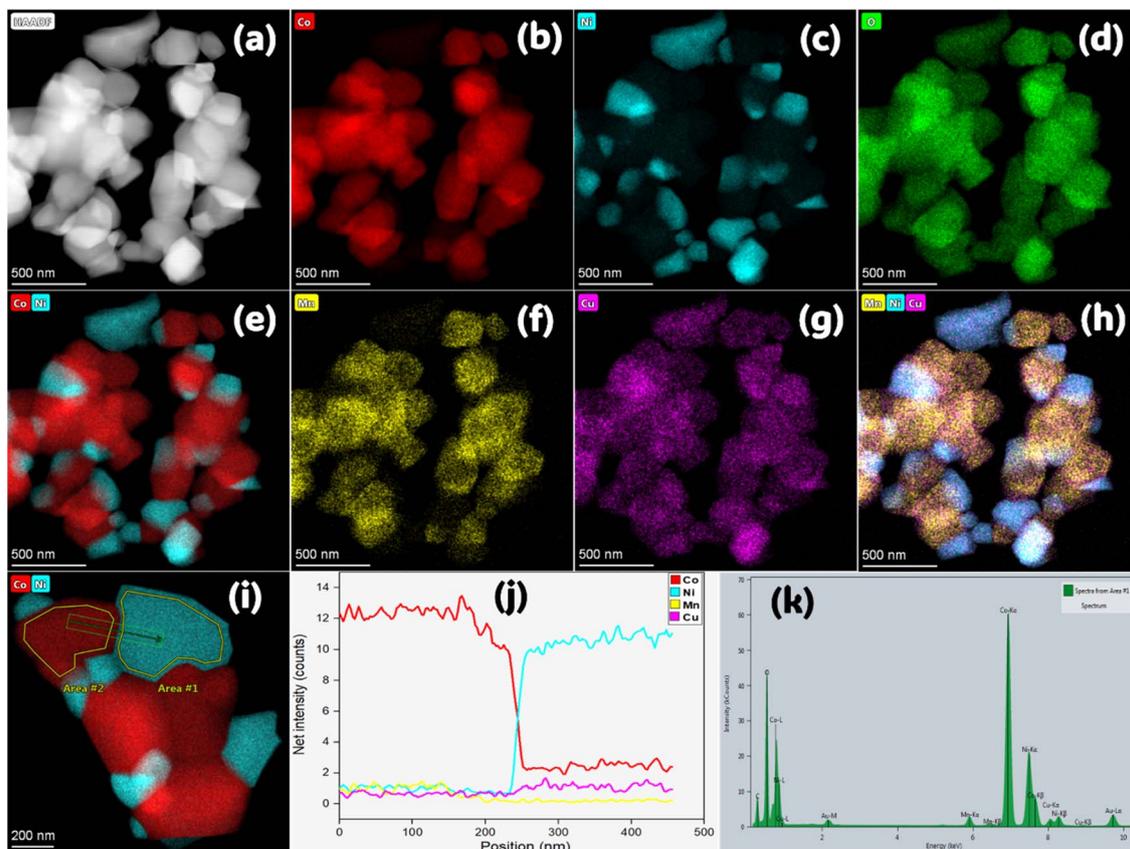
29492 | *J. Mater. Chem. A*, 2025, **13**, 29486–29503

This journal is © The Royal Society of Chemistry 2025

Fig. 7 Mn/Cu-doped Co_3O_4/NiO sample: (a) HAADF electron image; (b–e) corresponding EDS elemental distribution maps for Co, Ni, and O, and Co and Ni combined, respectively; (f–h) EDS maps for Mn, Cu, and combination of Mn, Ni and Co, respectively; (i) high magnification map showing Co and Ni distribution; (j) EDS line scan along arrow drawn in (i) (Mn and Cu signals ×2 for clarity); (k) general EDS spectrum.
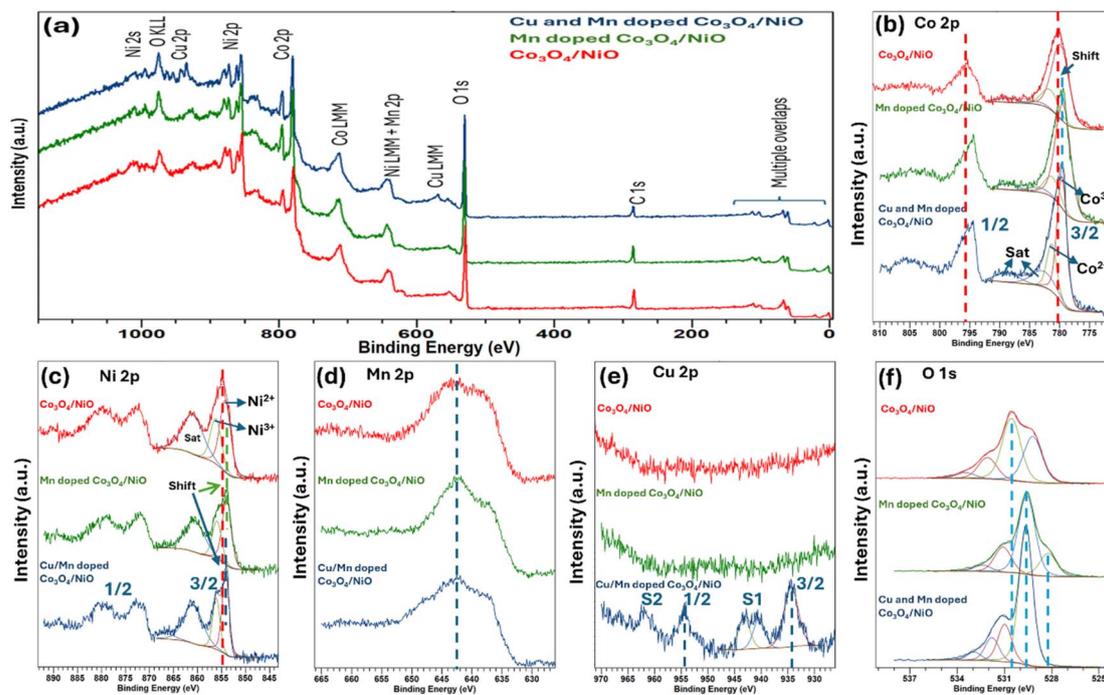

Fig. 8 XPS analysis of the composites: (a) wide-scan survey spectrum revealing the presence of Co, Ni, Mn, Cu, and O; (b–f) high-resolution core-level spectra of (b) Co 2p, (c) Ni 2p, (d) Mn 2p, (e) Cu 2p, and (f) O 1s regions, highlighting their respective chemical states and deconvoluted profiles.

This journal is © The Royal Society of Chemistry 2025

J. Mater. Chem. A, 2025, **13**, 29486–29503 | **29493**

Table 4 Atomic ratios of Ni^{2+}/Ni^{3+} and Co^{2+}/Co^{3+} calculated from XPS spectra

Sample	Atomic ratios of deconvoluted Ni $2p_{3/2}$		Atomic ratios of deconvoluted Co $2p_{3/2}$	
	Ni^{2+}	Ni^{3+}	Co^{2+}	Co^{3+}
Co_3O_4/NiO	1.59	1	1	3.82
Mn-doped Co_3O_4/NiO	1.75	1	1	5.13
Cu/Mn-doped Co_3O_4/NiO	1.59	1	1	2.68

combination of vacancies and oxygen ions, as is indeed shown in the analysis of the impedance spectroscopy results, discussed below. The XPS feature for O 1s, as shown in Fig. 9(f), is deconvoluted into several peaks. The lattice oxygen peak in the undoped, Mn-doped, and Mn/Cu-doped samples is present at 529.2 eV, 529.6/528.4 eV and 529.6 eV, respectively. A small peak at 528.4 eV in the Mn-doped sample can be assigned to lattice oxygen in the NiO with increased Ni^{2+}/Ni^{3+} ratio.[71] The peak at

530.6 eV in the Co_3O_4/NiO sample can be assigned to surface oxygen species[72] and is seen at 531.1 eV in the Mn- and Mn/Cu-doped materials.[73] The remaining deconvoluted peaks at 531.5 eV,[73,74] 532.1 eV,[75] 532.7 eV,[65,67] and 533.4 eV[75] can be assigned to adsorbed oxygen-containing surface species, such as hydroxyl groups and water molecules.

3.6. Electrochemical impedance spectroscopy

Electrochemical impedance spectroscopy (EIS) spectra were recorded on symmetrical cells based on GDC electrolytes and using each of the three composite materials in turn as both electrodes. Generally, the EIS spectra typically consisted of up to three discernible semicircular arcs in the high-frequency (HF), medium-frequency (MF), and low-frequency (LF) domains. The HF region predominantly reflects the intrinsic characteristics of the bulk material, including charge carrier transport (electronic or ionic conduction) through the ceramic grain matrix. The MF region typically encompasses contributions from grain boundary phenomena, particularly grain boundary resistance
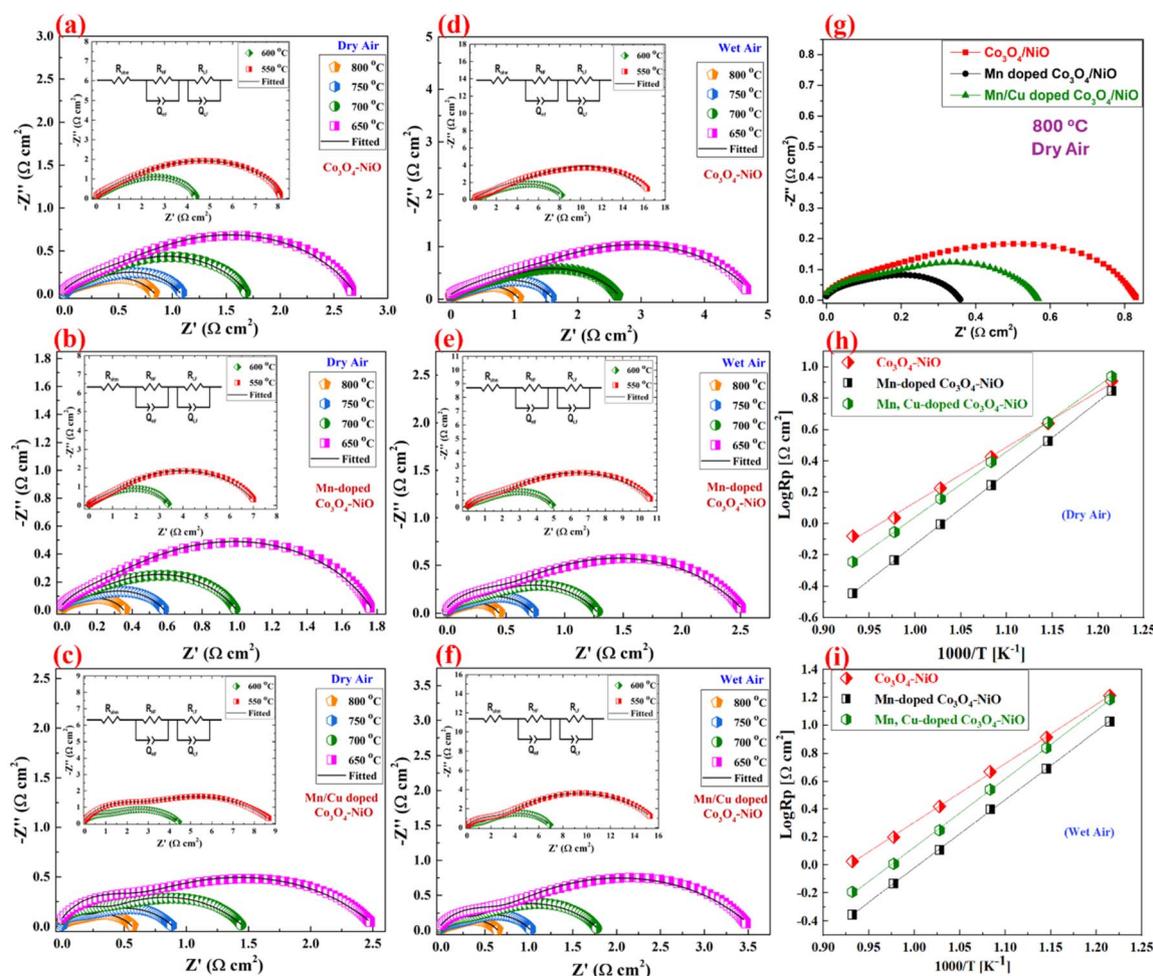

Fig. 9 Electrochemical impedance spectroscopy analysis of symmetrical cells employing each of the three composites at both electrodes: (a–c) Nyquist plots for Co_3O_4/NiO, Mn-doped Co_3O_4/NiO, and Mn/Cu-doped Co_3O_4/NiO, respectively, measured in dry air; (d–f) corresponding Nyquist plots in humidified air. (g) Comparison of Nyquist plots at 800 °C under dry air; (h) Arrhenius-type plots for all composites in dry air. (i) Arrhenius-type plots in humidified air.

29494 | *J. Mater. Chem. A*, 2025, **13**, 29486–29503

This journal is © The Royal Society of Chemistry 2025

and its corresponding capacitance, which can substantially influence and elevate the overall impedance due to their inherently higher resistive nature compared to the bulk. The LF region is predominantly governed by interfacial electrochemical processes at the electrode–electrolyte boundary, such as charge transfer kinetics and diffusional mass transport processes.[76,77] To facilitate quantitative interpretation, the impedance spectra are modelled using equivalent electrical circuits (EECs). The adopted EEC framework comprises three in-series subcircuits, each consisting of a resistor in parallel with a constant phase element (CPE).

The impedance corresponding to a CPE is expressed by the formula:

$$Z_{CPE_i} = \frac{1}{2\pi f_o C_i} \left(\frac{f_o}{jf}\right)^{\alpha}$$

where f = frequency, f_o = reference frequency, set to 1000 Hz, j = imaginary unit, C_i = capacitance at reference frequency, i is CPE number, α = coefficient with a value between 0.5 and 1.[78]

The EIS measurements were performed in both dry and humidified air (3 vol% H_2O) at temperatures between 550 and 800 °C, with precise gas flow regulation via a mass flow controller. Fig. 9(a–c) illustrate the experimental and fitted impedance spectra for Co_3O_4/NiO, Mn-doped Co_3O_4/NiO, and Mn/Cu co-doped Co_3O_4/NiO cathodes under dry conditions, while Fig. 9(d–f) presents the corresponding data obtained in humidified air. All three cathode materials exhibited favorable electrochemical performance at 800 °C, with notably reduced area-specific resistance (ASR) values in dry air. The impedance spectra were fitted using the equivalent circuit model depicted in the insets of Fig. 9(a–f) in order to extract individual ASR values. Both doped composites – the Mn-doped and Mn/Cu-doped composites – showed lower polarisation resistance than the undoped material. The Mn-doped Co_3O_4/NiO electrode demonstrated the best performance, achieving the lowest polarization resistances in both atmospheres (0.38 Ω cm^2 in dry air; 0.44 Ω cm^2 in wet air, at 800 °C). If any material were to have both protonic and electronic conductivity, it would be expected to show reduced ASR values in humidified air compared to dry air. Such a decrease in ASR under humidified conditions is attributed to the formation of a hydrated surface layer on the electrode and electrolyte, promoting proton mobility by lowering H^+ ion transport activation barriers. Furthermore, adsorbed water is reported to enhance catalytic activity at the

triple-phase boundaries, accelerating oxygen reduction kinetics and reducing polarization losses.[76] But in the current study, all three samples showed slightly higher ASR values in wet air than in dry air, implying that these samples do not have significant protonic conductivity.

The exceptional performance of the Mn-doped Co_3O_4/NiO may arise from the catalytic role of Mn in the oxygen reduction reaction and/or its role in refining the microstructure of the composite. Microstructural analysis by SEM, N_2 physisorption and DLS revealed a more homogeneous and finer grain morphology in the Mn-doped composite, which would act to expand the electrochemically active surface area and may also improve gas diffusion pathways. In the comparison of the EIS spectra for all three composites at 800 °C (Fig. 9(g)) the reduction in overall impedance is clearly visible for the co-doped and especially Mn-doped composite electrodes. The Arrhenius-type plots in Fig. 9(h) and (i) make clear that the Mn-doped sample has the lowest polarisation ASR at all experimental temperatures. The doubly-doped material is next, followed by the undoped material which generally has the highest R_ps, although there is some overlap with the doubly-doped material at the lowest temperatures.

The ASR values of these Co_3O_4-based composites at temperatures of 700–800 °C are presented together with recently reported work on Co_3O_4/GDC composite cathodes for SOFCs[79] in Table 5, and can be seen to compare favourably.

In Table 6 the ASR values of these composites are also compared with some other reported studies carried out under similar conditions, to demonstrate the importance of the study. This comparison shows that Mn-doped Co_3O_4/NiO exhibits the lowest ASR value, implying that it has the better electrochemical performance and is a promising cathode material for IT-SOFCs.

3.7. Distribution of relaxation time study

Electrochemical processes often manifest as overlapping features in Nyquist plots, appearing as single semicircular arcs that obscure several individual mechanistic contributions. To address this limitation, the DRT method has emerged as a pivotal analytical tool, enabling the deconvolution of physicochemically distinct processes through their characteristic relaxation times (τ) – parameters intrinsically linked to reaction kinetics and charge-transfer dynamics. Unlike is often the case in conventional equivalent circuit modelling, the number of

Table 5 Comparison of ASR values with relevant literature

Cathode	Electrolyte	Temperature (°C)	ASR (Ω cm^2)	Ref.
Co_3O_4/GDC	YSZ	700	1.19	79
Co_3O_4/GDC	YSZ	750	0.88	79
Co_3O_4/GDC	YSZ	800	0.68	79
Co_3O_4/NiO	GDC	800	0.83	This work
Mn/Cu-doped Co_3O_4/NiO	GDC	800	0.57	This work
Mn-doped Co_3O_4/NiO	GDC	700	0.98	This work
Mn-doped Co_3O_4/NiO	GDC	750	0.58	This work
Mn-doped Co_3O_4/NiO	GDC	800	0.38	This work

This journal is © The Royal Society of Chemistry 2025

J. Mater. Chem. A, 2025, **13**, 29486–29503 | **29495**

Table 6 Comparison of performance of Co_3O_4/NiO materials from this work with literature reports of other composites evaluated under similar conditions

Electrode (abbreviation)	Electrolyte	Atmosphere – temperature (°C)	ASR (Ω cm^2)	Ref.
$La_{0.65}Bi_{0.1}Sr_{0.25}Cr_{0.5}Fe_{0.5}O_3$/SDC (LBSCF/SDC)	LSGM	Air-800	2.90	80
$La_{0.8}Sr_{0.2}MnO_{3−\delta}$/GDC (LSM/GDC)	YSZ	Air-800	1.44	81
$La_{0.75}Sr_{0.25}Cr_{0.5}Mn_{0.5}O_{3−\delta}$/YSZ (LSCM/YSZ)	YSZ	Air-800	0.43	82
$La_{5.5}WO_{11.25−\delta}/La_{0.8}Sr_{0.2}MnO_{3+\delta}$ (LWO/LSM)	LWO	Wet air-750	1.4	83
$La_{0.5}Sr_{1.5}MnO_{4+\delta}$/SDC (LSM/SDC)	LSGM	Air-800	0.813	84
$(La_{0.5}Sr_{1.5}Mn)Ni_{0.1}O_{4+\delta}$/SDC (LSMN/SDC)	LSGM	Air-800	0.676	84
Co_3O_4/NiO	GDC	800	0.83	This work
Mn/Cu-doped Co_3O_4/NiO	GDC	800	0.57	This work
Mn-doped Co_3O_4/NiO	GDC	700	0.98	This work
Mn-doped Co_3O_4/NiO	GDC	750	0.58	This work
Mn-doped Co_3O_4/NiO	GDC	800	0.38	This work

peaks in the DRT plots corresponds to the number of processes taking place.[85]

DRT plots were obtained from the deconvolution of the EIS spectra in order to identify the different physio-chemical processes, and examine their contribution to the overall resistance of the cell. All DRT plots showed five distinct physio-chemical processes as shown in Fig. 10. Zhang and co-workers got similar results for their symmetrical cell and made assignments of their peaks to different physio-chemical processes.[86] For the system described in the current work, the assignment of these peaks is presented in Table 7.

The DRT plots of all the samples under dry and wet air conditions are shown in Fig. 10. Notably, the intensities and positions of these peaks vary with composition, suggesting that the dopants and structural modifications in the cathode material influence the rates and energetics of each process. These findings underscore the importance of carefully tuning cathode formulations to improve their electrochemical performance, as even minor compositional differences can significantly alter the overall polarisation behaviour. In addition, the sensitivity of certain peaks to the operating atmosphere (dry vs. wet air) further emphasizes the role of moisture content in modulating key reaction pathways. Taken together, the DRT analyses provide crucial insights into the underlying mechanisms that govern cell performance, thereby offering a valuable framework for designing next-generation SOFC cathodes with enhanced stability and catalytic efficiency.
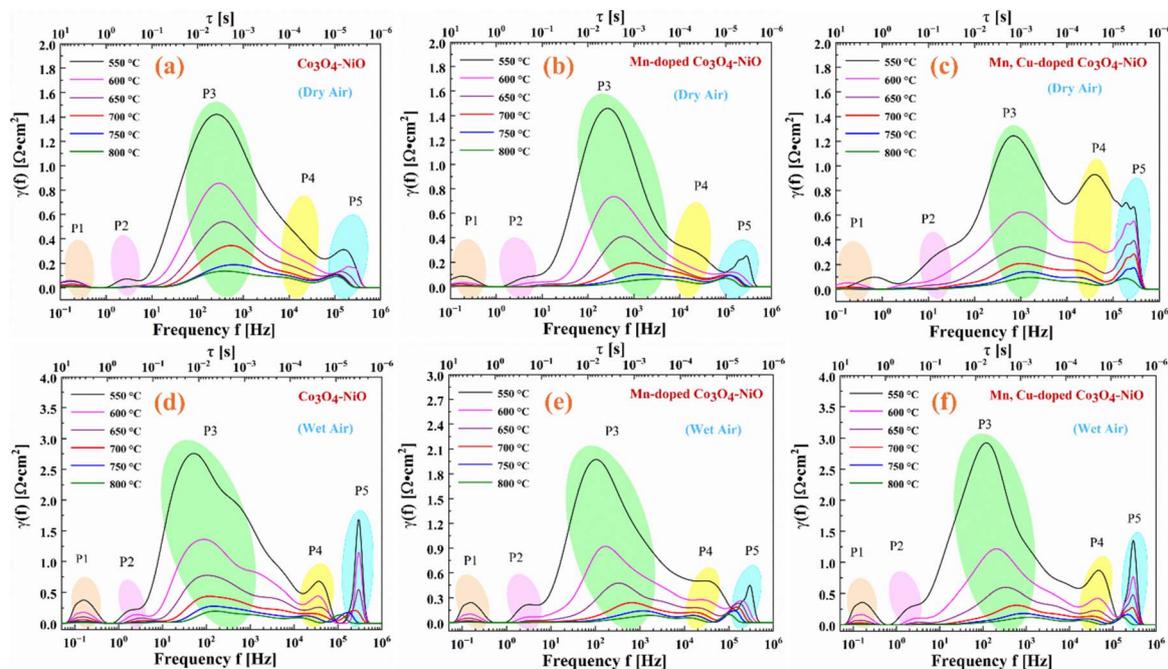

Fig. 10 Distribution of Relaxation Time (DRT) analysis derived from electrochemical impedance spectra of the composites: (a–c) DRT profiles of Co_3O_4/NiO, Mn-doped Co_3O_4/NiO, and Mn/Cu-doped Co_3O_4/NiO in dry air, resolving constituent electrochemical processes; (d–f) corresponding DRT profiles in wet air, illustrating humidity-dependent relaxation behaviour.

29496 | J. Mater. Chem. A, 2025, **13**, 29486–29503

This journal is © The Royal Society of Chemistry 2025

Table 7 Peak assignment (P1 to P5) in the DRT graphs

Peak	Frequency (Hz)	Process
P1	0.005–1	Molecular oxygen adsorption on the cathode
P2	1–17	Dissociation of O_2 into adsorbed oxygen atoms
P3	20–10 000	Formation of adsorbed oxygen ion
P4	2500–54 000	Combination of oxygen ions and oxygen vacancies
P5	>28 000	Oxygen vacancy diffusion

As the temperature increases, the relaxation processes associated with the ORR (P3) for these composite cathodes become progressively faster, as evidenced by the systematic shift of this peak towards higher frequencies (*i.e.*, shorter relaxation times). In addition, the relative peak intensities for P3 tend to diminish, suggesting a significant reduction in the contribution to the overall resistance from the respective processes. These observations collectively indicate that elevated temperatures enhance the electrochemical activity by promoting more efficient charge transport and faster reaction rates, a desirable effect for optimizing SOFC cathode performance. Along with enhanced ORR kinetics at higher temperatures, the other processes contributing to the overall performance of the cell also show improvements in the adsorption of oxygen molecules on the surface of the composites (P1), its dissociation into oxygen atoms (P2), occupation of vacancies by oxygen ions (P4) and diffusion of the oxygen vacancies (P5), as the temperature is increased from 550 to 800 °C.

Fig. 11(a and b) compares the DRT plots for all three composites at 750 and 800 °C. Considering the ORR process (P3) and the combination of adsorbed oxygen ions and oxygen vacancies (P4), the Mn-doped Co_3O_4/NiO clearly shows a much smaller contribution than the other composites towards the overall impedance at both temperatures, indicating lower
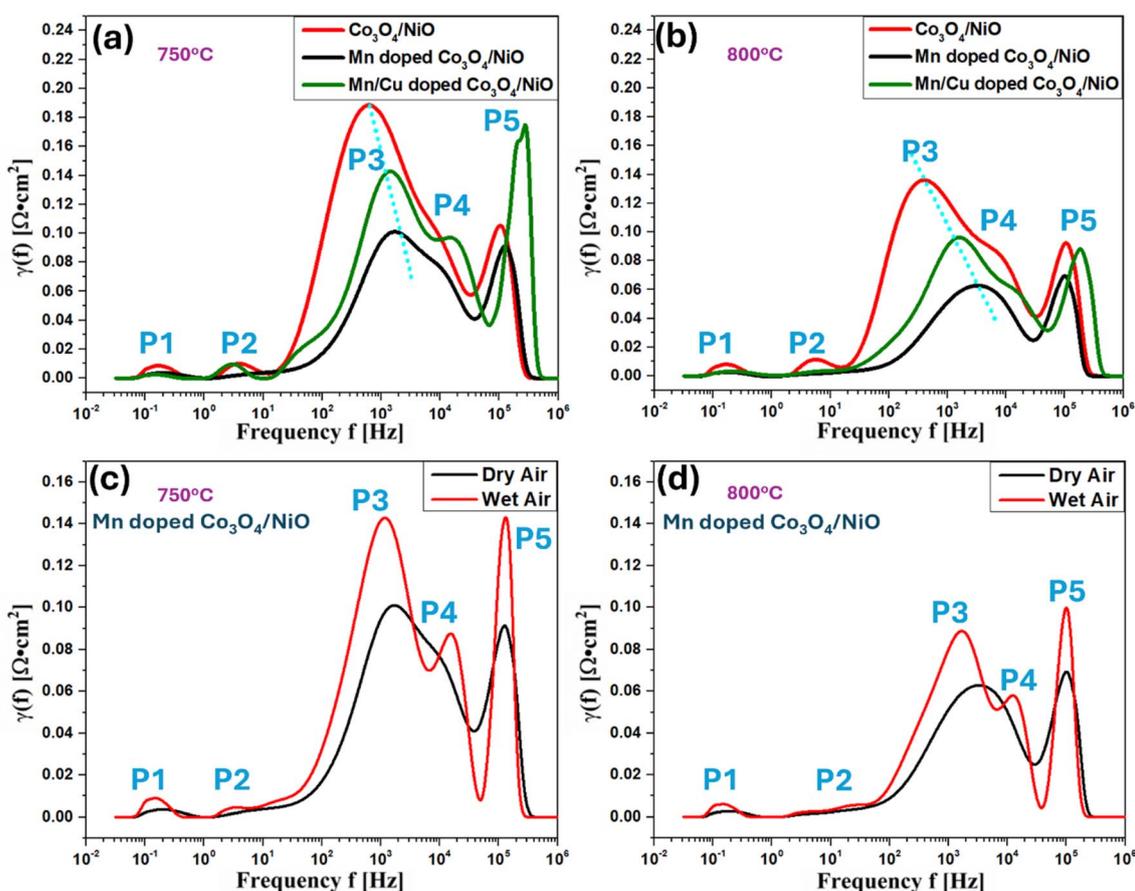

Fig. 11 Comparative Distribution of Relaxation Time (DRT) analysis of the composites under varying conditions, showing contributions from processes P1–P5 (see text for details): (a) DRT profiles of the 3 composites in dry air at 750 °C; (b) corresponding DRT comparison at 800 °C in dry air. Comparison of DRT plots in dry *vs.* wet air for Mn-doped Co_3O_4/NiO at (c) 750 °C, and (d) 800 °C, emphasizing the effect of humidity on relaxation processes.

This journal is © The Royal Society of Chemistry 2025

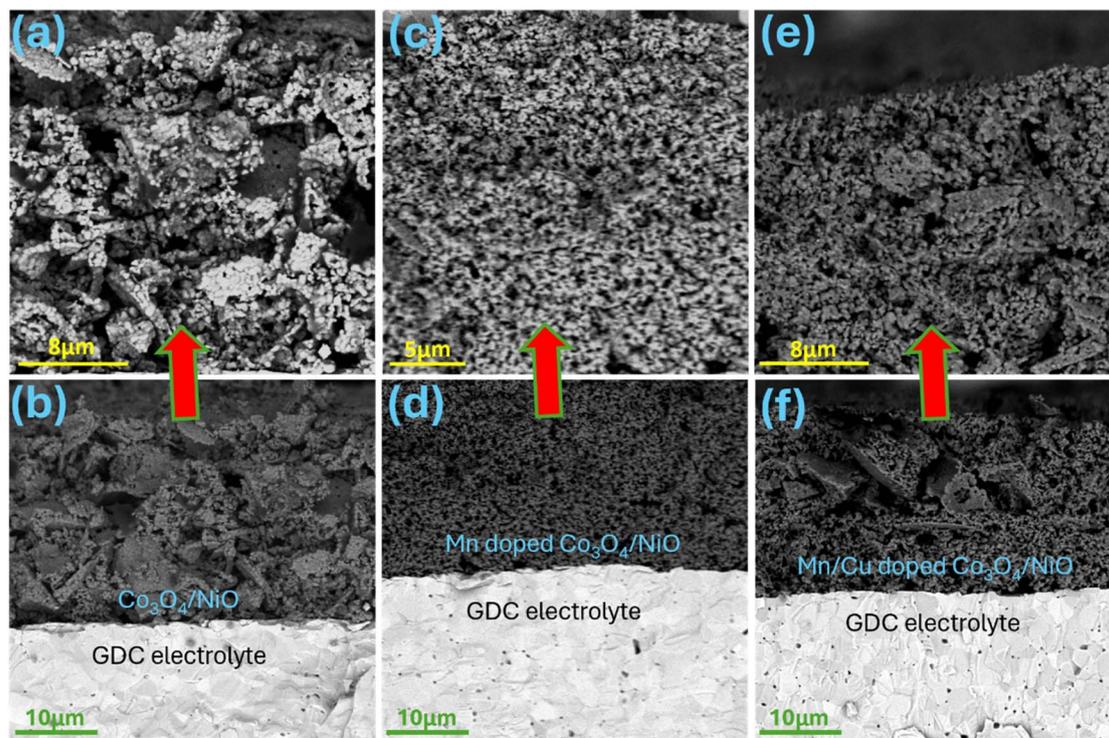*J. Mater. Chem. A*, 2025, **13**, 29486–29503 | **29497**

Fig. 12 Structural and morphological characterisation of the composite/GDC interface regions of the symmetrical cells after electrochemical testing by SEM: (a, c and d) High magnification micrographs of the composite electrodes (GDC excluded), revealing distinct grain morphology and porosity; and (b, d f) cross-sectional images of Co_3O_4/NiO, Mn-doped Co_3O_4/NiO and Mn/Cu-doped Co_3O_4/NiO, respectively (with GDC).

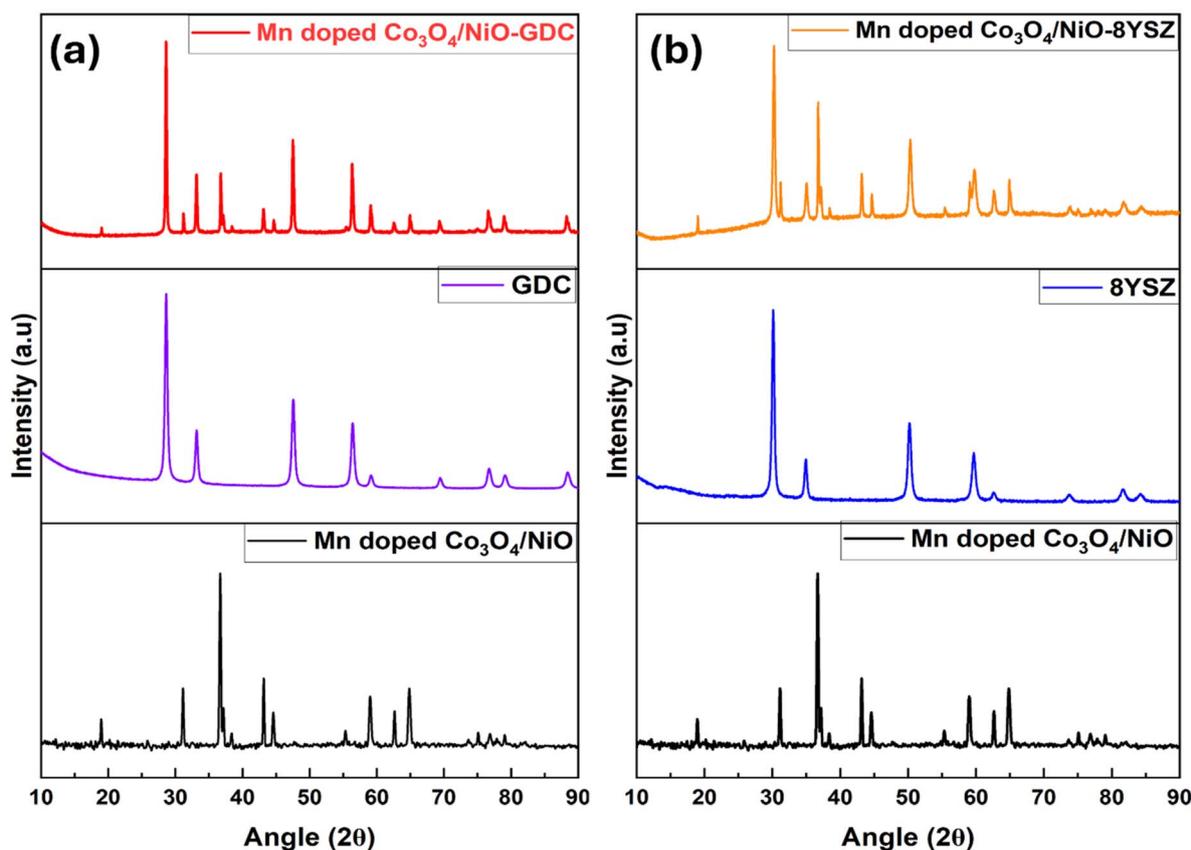**Fig. 13** Phase stability evaluation of Mn-doped Co_3O_4/NiO after thermal aging at 800 °C for 100 h. Comparison of XRD patterns for Mn-doped Co_3O_4/NiO aged with (a) GDC; and (b) YSZ, demonstrating chemical compatibility under prolonged high-temperature conditions. In each case, aged mixtures (top pattern) are compared with fresh electrolyte (middle) and fresh cathode materials (bottom).

29498 | *J. Mater. Chem. A*, 2025, **13**, 29486–29503

This journal is © The Royal Society of Chemistry 2025

energy barriers for these processes. Also, at both temperatures, there is a clear shift towards higher frequency (or small time constant for the relaxation process) for the Mn-doped composite, implying faster reaction kinetics, and making this material a potential candidate for SOFC cathodes. Fig. 11(c and d) is a comparison of the DRT graphs of Mn-doped Co_3O_4/NiO obtained in dry and wet air conditions at 750 and 800 °C. Very clearly, the results obtained in the dry air show less contribution towards the overall impedance for all processes, P1–P5, and display faster kinetics, for processes P1–P3, compared to the results in wet air. Adsorption of water on the surface of the composites can limit the number of available surface sites for the adsorption of molecular oxygen (P1), which can act as a rate-limiting step in this case and so adversely affect all the other processes, at steady state.

3.8. Post-test analysis of symmetrical cells

Fig. 12 shows the scanning electron microscopy images of the cross-section of symmetrical cells in which the three composites are deposited on both surfaces of GDC electrolytes after they had been used in the electrochemical experiments. All the samples showed good contact between the electrode and the electrolyte. In the undoped Co_3O_4/NiO (Fig. 12(a)) and the Cu/Mn-doped Co_3O_4/NiO materials (Fig. 12(g)) the composite electrodes are observed to contain agglomerates. In comparison, the Mn-doped Co_3O_4/NiO electrode shows a more

uniform, less agglomerated porous structure in good contact with the GDC electrolyte.

3.9. Long-term chemical compatibility study of the composite electrode with selected electrolytes

To evaluate the chemical compatibility and thermal stability of the synthesized Mn-doped Co_3O_4/NiO composite for application as an SOFC cathode, equal mass mixtures of the composite with GDC and YSZ electrolytes were subjected to thermal treatment at 800 °C for 100 h. Post-annealing X-ray diffraction (XRD) analysis, as illustrated in Fig. 13(a) and (b), revealed no detectable interfacial reactions or secondary phase formation. The diffraction patterns exclusively exhibited peaks corresponding to the parent composite and the electrolyte phases, confirming the absence of undesirable chemical reactions. Furthermore, the Mn-doped Co_3O_4/NiO composite retained its original phase composition under these conditions with no evidence of decomposition or impurity peaks. This demonstrates excellent phase stability and compatibility with both GDC and YSZ electrolytes at SOFC operating temperatures, fulfilling critical material requirements for long-term device reliability.

3.10. Extended electrochemical study of symmetrical cell

A long-term electrochemical test of a symmetrical cell, Mn-doped Co_3O_4–NiO|GDC|Mn-doped Co_3O_4–NiO, was performed
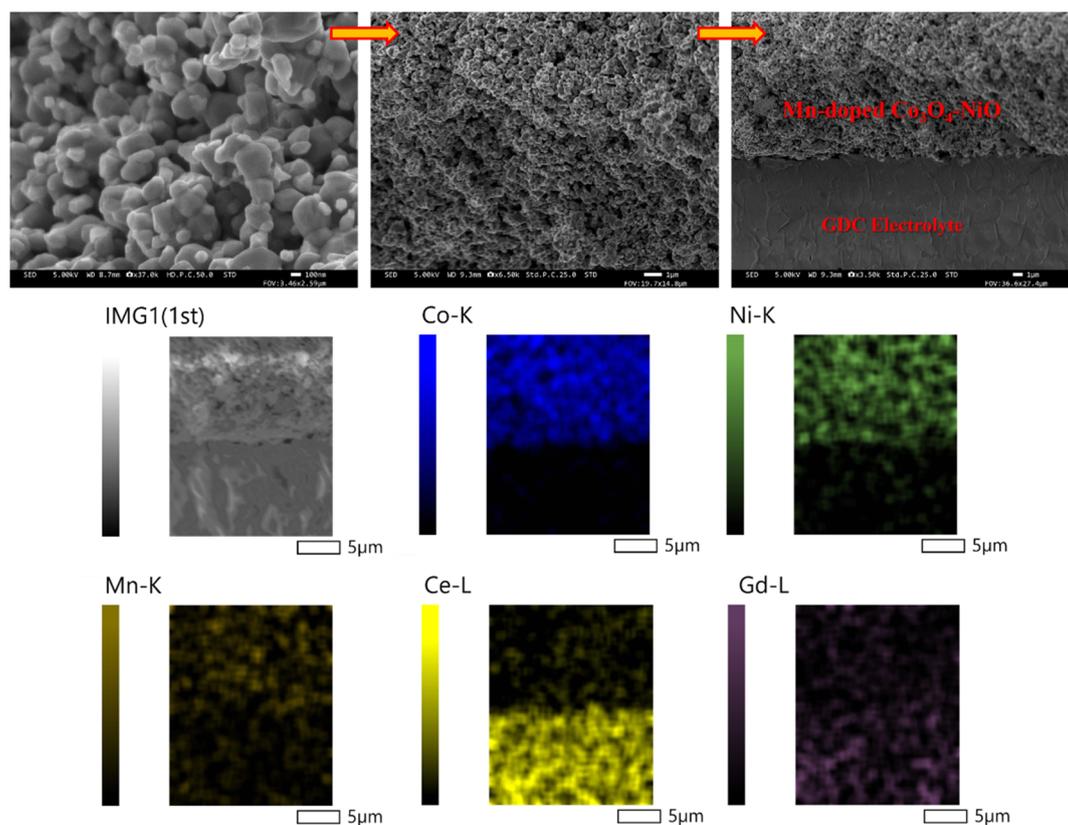
Fig. 14 SEM and EDS mapping study of the symmetrical cell, Mn-doped Co_3O_4–NiO|GDC|Mn-doped Co_3O_4–NiO, after 100 h electrochemical test.

This journal is © The Royal Society of Chemistry 2025

J. Mater. Chem. A, 2025, **13**, 29486–29503 | **29499**

in air at 800 °C for a period of 100 h. The EIS results obtained showed that the cell remained relatively stable over this time period, with an increase in polarization resistance, R_p, of around 18% after 100 h, as shown in Fig. S2.

After the long term electrochemical test, the used symmetrical cell was studied in cross-section using SEM and EDS mapping (Fig. 14). The SEM images of the cross-section and surface of the electrode show excellent porosity and small particle size were retained over the 100 h test. The electrode layer remains tightly bonded, and no evidence for intermediate layers or products of chemical reaction was observed between the electrolyte and the electrode in the used cell. The EDS study shows the expected distribution of the elements – Co, Ni and Mn in the cathode layer and Ce and Gd in the electrolyte – with no impurities or inter-diffusion, after the long-term test.

4. Conclusions

The integration of Mn into Co_3O_4–NiO composites significantly enhances their viability as SOFC cathodes through structural refinement and catalytic activation. XRD and EDS mapping confirmed the preferential substitution of Mn in the Co_3O_4 phase, which reduced crystallite sizes and increased surface area, while co-doping of Mn and Cu introduced microstructural heterogeneity. Electrochemical assessments revealed the Mn-doped composite's exceptional performance, with ASR values 56% lower than for the undoped material at 800 °C, attributed to its porous morphology and optimized triple-phase boundaries. DRT analysis further elucidated humidity-dependent kinetics, indicating suppressed oxygen adsorption in wet air and the dominance of electronic conduction. Stability studies confirmed excellent compatibility with GDC and YSZ, critical for long-term operation. Compared to literature benchmarks, the Mn-doped variant's ASR ($0.38 \ \Omega \ cm^2$) surpasses recent Co_3O_4/GDC composites ($0.68 \ \Omega \ cm^2$), underscoring its superiority. These results advocate for Mn-doped Co_3O_4–NiO as a practicable and active cathode material. Future work will focus on integration of these composite materials into full SOFC cells, including the selection and optimization of a chemically and mechanically compatible anode, selection of interconnect materials, and cell architecture, as well as exploration of a third, proton-conducting phase to form a triple-conducting composite, with the aim of moving towards real world SOFC applications. The study will also encompass long-term load-cycling experiments and comprehensive evaluation of electrochemical durability to ensure sustained operational reliability.

This study advances the rational design of doped transition-metal oxide composites for next-generation energy conversion technologies.

Author contributions

Shah: conceptualisation; methodology; investigation; formal analysis; writing – original draft; writing – reviewing & editing. Sultan: investigation; formal analysis; writing – original draft; writing – reviewing & editing. Zheng: supervision; writing – reviewing & editing. Sajjad: supervision; funding acquisition. Baker: conceptualisation; supervision; methodology; resources; formal analysis; project administration; writing – reviewing & editing; funding acquisition.

Conflicts of interest

There is no conflict of interest associated with the work presented here.

Data availability

Key data underpinning this article are available on the PURE repository of the University of St Andrews at: **https://research-portal.st-andrews.ac.uk/en/persons/richard-baker/datasets/**.

Supplementary information covering the estimation of particle size from the BET data, the electrical conductivity of the materials studied, results of extended electrochemical testing and evaluation of compatibility with a second electrolyte material is available. See DOI: **https://doi.org/10.1039/d5ta03764f**.

Acknowledgements

References

1 T. Kober, H. W. Schiffer, M. Densing and E. Panos, Global energy perspectives to 2060–WEC's World Energy Scenarios 2019, *Energy Strategy Rev.*, 2020, **31**, 100523.

2 J. Li, J. Cheng, Y. Zhang, Z. Chen, M. Nasr, M. Farghali and A. I. Osman, Advancements in Solid Oxide Fuel Cell Technology: Bridging Performance Gaps for Enhanced Environmental Sustainability, *Adv. Energy Sustainability Res.*, 2024, **5**(11), 2400132.

3 A. B. Stambouli and E. Traversa, Solid oxide fuel cells (SOFCs): a review of an environmentally clean and efficient source of energy, *Renew. Sust. Energy Rev.*, 2002, **6**(5), 433–455.

4 S. Z. Golkhatmi, M. I. Asghar and P. D. Lund, A review on solid oxide fuel cell durability: latest progress, mechanisms, and study tools, *Renew. Sust. Energy Rev.*, 2022, **161**, 112339.

5 M. Zhang, G. Jeerh, P. Zou, R. Lan, M. Wang, H. Wang and S. Tao, Recent development of perovskite oxide-based electrocatalysts and their applications in low to

29500 | *J. Mater. Chem. A*, 2025, **13**, 29486–29503

This journal is © The Royal Society of Chemistry 2025

intermediate temperature electrochemical devices, *Mater. Today*, 2021, **49**, 351–377.

6 P. Koteswararao, B. M. Suresh, B. N. Wani and P. V. B. Rao, Review on different components of solid oxide fuel cells, *J. Powder Metall. Min*, 2017, **6**, 181.

7 A. K. Yadav, S. Sinha and A. Kumar, Advancements in composite cathodes for intermediate-temperature solid oxide fuel cells: a comprehensive review, *Int. J. Hydrogen Energy*, 2024, **59**, 1080–1093.

8 J. M. Serra, S. Uhlenbruck, W. A. Meulenberg, H. P. Buchkremer and D. Stöver, Nano-structuring of solid oxide fuel cells cathodes, *Top. Catal.*, 2006, **40**(1), 123–131.

9 J. M. Serra and H. P. Buchkremer, On the nanostructuring and catalytic promotion of intermediate temperature solid oxide fuel cell (IT-SOFC) cathodes, *J. Power Sources*, 2007, **172**(2), 768–774.

10 S. Lee and K. Gerdes, Functional nanostructure engineering of SOFC cathode by solution infiltration, *ECS Electrochem. Lett.*, 2015, **4**(3), F17.

11 L. Baqué, A. Caneiro, M. S. Moreno and A. Serquis, High performance nanostructured IT-SOFC cathodes prepared by novel chemical method, *Electrochem. Commun.*, 2008, **10**(12), 1905–1908.

12 D. Ding, X. Li, S. Y. Lai, K. Gerdes and M. Liu, Enhancing SOFC cathode performance by surface modification through infiltration, *Energy Environ. Sci.*, 2014, **7**(2), 552–575.

13 S. U. Rehman, A. Shaur, R. H. Song, T. H. Lim, J. E. Hong, S. J. Park and S. B. Lee, Nano-fabrication of a high-performance $LaNiO_3$ cathode for solid oxide fuel cells using an electrochemical route, *J. Power Sources*, 2019, **429**, 97–104.

14 P. A. Connor, X. Yue, C. D. Savaniu, R. Price, G. Triantafyllou, M. Cassidy and J. T. Irvine, Tailoring SOFC electrode microstructures for improved performance, *Adv. Energy Mater.*, 2018, **8**(23), 1800120.

15 W. Jia, Y. Wang, J. Huang, M. Li, B. Xiang, Y. Wang and L. Ge, Alternative B-site-doped $La_{0.6}Sr_{0.4}Co_{0.2}Fe_{0.8-x}M_xO_3$ (M= Ni, Cu, Nb; x= 0, 0.1, 0.2) as innovative cathode material for LT-SOFC with enhanced charge transfer and oxygen ion diffusion, *Appl. Energy*, 2024, **353**, 122096.

16 J. Nisar, G. Kaur, S. Giddey, S. Bhargava and L. Jones, Cathode Materials for Intermediate Temperature Solid Oxide Fuel Cells, *Fuels*, 2024, **5**(4), 805–824.

17 J. Qi, C. Yuan, H. Ye, P. Shan, S. Li, S. He and Y. Zheng, Tailoring the catalytic activity of $PrBaFe_2O_{5+\delta}$ cathode material with non-transition metal In-doping for solid oxide fuel cells, *J. Eur. Ceram. Soc.*, 2025, **45**(3), 117057.

18 J. Zhang, P. Yao, X. Lu, J. Chen, W. Liu, Y. Zhao and Y. Li, Surface decoration of $Pr_{1.7}Sr_{0.3}Ni_{0.7}Cu_{0.3}O_{4+\delta}$ Ruddlesdene-Popper perovskite cathode with $BaPrO_{3-\delta}$ nanoparticles by Ba doping for protonic ceramic fuel cells, *Int. J. Hydrogen Energy*, 2025, **98**, 1044–1051.

19 S. Yang, Y. Gu and S. Yu, The effect of Mo and Sc dopants on the performance of an $Sr_2Fe_2O_6$ cathode for use in proton-conducting solid oxide fuel cells, *Mater. Sci. Eng., B*, 2025, **311**, 117836.

20 X. Jiang, X. Zhou, L. Liu, M. Fang, B. Zhang, Y. Tang and H. Liu, Electrochemical performance of a low-temperature solid oxide fuel cells with cobalt-based perovskite as the cathode, *Mater. Sci. Eng., B*, 2025, **313**, 117941.

21 H. Qi, T. Zhang, P. Qiu, D. Liu, B. Tu and M. Cheng, Comparison of nanostructured composite cathodes synthesized by liquid self-assembly and nanosolid mechanical-mixing for solid oxide fuel cell, *Int. J. Hydrogen Energy*, 2022, **47**(35), 15721–15730.

22 Y. M. Park, J. H. Kim and H. Kim, High-performance composite cathodes for solid oxide fuel cells, *Int. J. Hydrogen Energy*, 2011, **36**(15), 9169–9179.

23 N. T. Hart, N. P. Brandon, M. J. Day and N. Lapena-Rey, Functionally graded composite cathodes for solid oxide fuel cells, *J. Power Sources*, 2002, **106**(1–2), 42–50.

24 H. G. Desta, G. Gebreslassie, J. Zhang, B. Lin, Y. Zheng and J. Zhang, Enhancing performance of lower-temperature solid oxide fuel cell cathodes through surface engineering: a review, *Prog. Mater. Sci.*, 2024, 101353.

25 Y. Liang, Y. Li, H. Wang, J. Zhou, J. Wang, T. Regier and H. Dai, Co_3O_4 nanocrystals on graphene as a synergistic catalyst for oxygen reduction reaction, *Nat. Mater.*, 2011, **10**(10), 780–786.

26 T. Zhang, C. He, F. Sun, Y. Ding, M. Wang, L. Peng and Y. Lin, Co_3O_4 nanoparticles anchored on nitrogen-doped reduced graphene oxide as a multifunctional catalyst for H_2O_2 reduction, oxygen reduction and evolution reaction, *Sci. Rep.*, 2017, **7**(1), 43638.

27 D. Hassen, M. A. Shenashen, A. R. El-Safty, A. Elmarakbi and S. A. El-Safty, Anisotropic N-Graphene-diffused Co_3O_4 nanocrystals with dense upper-zone top-on-plane exposure facets as effective ORR electrocatalysts, *Sci. Rep.*, 2018, **8**(1), 3740.

28 Y. Wang, R. Gan, Z. Ai, H. Liu, C. Wei, Y. Song and J. Shi, Hollow Co_3O_{4x} nanoparticles decorated N-doped porous carbon prepared by one-step pyrolysis as an efficient ORR electrocatalyst for rechargeable Zn-air batteries, *Carbon*, 2021, **181**, 87–98.

29 C. Tomon, A. Krittayavathananon, S. Sarawutanukul, S. Duangdangchote, N. Phattharasupakun, K. Homlamai and M. Sawangphruk, Enhancing bifunctional electrocatalysts of hollow Co_3O_4 nanorods with oxygen vacancies towards ORR and OER for Li–O_2 batteries, *Electrochim. Acta*, 2021, **367**, 137490.

30 G. Cheng, T. Kou, J. Zhang, C. Si, H. Gao and Z. Zhang, O22-/O-functionalized oxygen-deficient Co_3O_4 nanorods as high performance supercapacitor electrodes and electrocatalysts towards water splitting, *Nano Energy*, 2017, **38**, 155–166.

31 J. Hao, S. Peng, H. Li, S. Dang, T. Qin, Y. Wen and G. Cao, A low crystallinity oxygen-vacancy-rich Co_3O_4 cathode for high-performance flexible asymmetric supercapacitors, *J. Mater. Chem. A*, 2018, **6**(33), 16094–16100.

32 S. U. Rehman, M. H. Hassan, S. Y. Batool, H. S. Kim, R. H. Song, T. H. Lim and S. B. Lee, A highly stable Co_3O_4-GDC nanocomposite cathode for intermediate temperature solid oxide fuel cells, *Int. J. Hydrogen Energy*, 2024, **51**, 1242–1254.

This journal is © The Royal Society of Chemistry 2025

J. Mater. Chem. A, 2025, **13**, 29486–29503 | **29501**

33 X. Yang, Y. Yin, S. Yu and L. Bi, Gluing $Ba_{0.5}Sr_{0.5}Co_{0.8}Fe_{0.2}O_{3-\delta}$ with Co_3O_4 as a cathode for proton-conducting solid oxide fuel cells, *Sci. China Mater.*, 2023, **66**(3), 955–963.

34 D. Chen, F. Wang and Z. Shao, Interlayer-free electrodes for IT-SOFCs by applying Co_3O_4 as sintering aid, *Int. J. Hydrogen Energy*, 2012, **37**(16), 11946–11954.

35 C. Zhang, Z. Du, H. Zhao and X. Zhang, Modification of electrocatalytic activity of $BaCe_{0.40}Sm_{0.20}Fe_{0.40}O_{3-\delta}$ with Co_3O_4 as cathode for proton-conducting solid oxide fuel cell, *Electrochim. Acta*, 2013, **108**, 369–375.

36 X. Zhao, J. Chang, D. Tian, A. B. Bayu, X. Lu, Y. Ding and H. Li, Enhanced performance of $Gd_{0.6}Sr_{0.4}FeO_{3-\delta}$ electrode by Co_3O_4 incorporation for symmetrical solid oxide fuel cells, *Mater. Lett.*, 2021, **295**, 129848.

37 H. Zhang, H. Liu, Y. Cong and W. Yang, Investigation of $Sm_{0.5}Sr_{0.5}CoO_{3-\delta}/Co_3O_4$ composite cathode for intermediate-temperature solid oxide fuel cells, *J. Power Sources*, 2008, **185**(1), 129–135.

38 N. Imanishi, R. Ohno, K. Murata, A. Hirano, Y. Takeda, O. Yamamoto and K. Yamahara, LSM-YSZ Cathode with Infiltrated Cobalt Oxide and Cerium Oxide Nanoparticles, *Fuel Cells*, 2009, **9**(3), 215–221.

39 G. Yang, W. Zhou, M. Liu and Z. Shao, Enhancing electrode performance by exsolved nanoparticles: a superior cobalt-free perovskite electrocatalyst for solid oxide fuel cells, *ACS Appl. Mater. Interfaces*, 2016, **8**(51), 35308–35314.

40 M. Liang, Y. Zhu, Y. Song, D. Guan, Z. Luo, G. Yang and Z. Shao, A new durable surface nanoparticles-modified perovskite cathode for protonic ceramic fuel cells from selective cation exsolution under oxidizing atmosphere, *Adv. Mater.*, 2022, **34**(10), 2106379.

41 P. Yao, J. Zhang, Q. Qiu, Y. Zhao, F. Yu and Y. Li, A dual modification strategy of highly active catalytic cathode for proton-conducting solid oxide fuel cell with Ni-doped $PrBaFe_{1.9}Mo_{0.1}O_{6-\delta}$, *J. Power Sources*, 2024, **606**, 234591.

42 H. Lee, H. Jung, C. Kim, S. Kim, I. Jang, H. Yoon and T. Song, Enhanced electrochemical performance and durability of the $BaCo_{0.4}Fe_{0.4}Zr_{0.1}Y_{0.1}O_{3-\delta}$ composite cathode of protonic ceramic fuel cells *via* forming nickel oxide nanoparticles, *ACS Appl. Energy Mater.*, 2021, **4**(10), 11564–11573.

43 M. Nadeem, B. Hu and C. Xia, Effect of NiO addition on oxygen reduction reaction at lanthanum strontium cobalt ferrite cathode for solid oxide fuel cell, *Int. J. Hydrogen Energy*, 2018, **43**(16), 8079–8087.

44 P. Jiang, Q. Wang, J. Dai, W. Li and Z. Wei, Fabrication of $NiO@Co_3O_4$ core/shell nanofibres for high-performance supercapacitors, *Mater. Lett.*, 2017, **188**, 69–72.

45 F. Chen, Y. Chi, H. Zhang, F. Ma and F. Qin, Band-gap shrinked $NiO@Co_3O_4$ nanotubes as high-performance supercapacitor electrodes, *J. Alloys Compd.*, 2021, **888**, 161463.

46 R. Kumar, S. M. Youssry, H. M. Soe, M. M. Abdel-Galeil, G. Kawamura and A. Matsuda, Honeycomb-like open-edged reduced-graphene-oxide-enclosed transition metal oxides (NiO/Co_3O_4) as improved electrode materials for high-performance supercapacitor, *J. Energy Storage*, 2020, **30**, 101539.

47 M. B. Askari, P. Salarizadeh, A. Beheshti-Marnani and A. Di Bartolomeo, $NiO-Co_3O_4$-rGO as an efficient electrode material for supercapacitors and direct alcoholic fuel cells, *Adv. Mater. Interfaces*, 2021, **8**(15), 2100149.

48 S. C. Sekhar, G. Nagaraju and J. S. Yu, High-performance pouch-type hybrid supercapacitor based on hierarchical $NiO-Co_3O_4$-NiO composite nanoarchitectures as an advanced electrode material, *Nano Energy*, 2018, **48**, 81–92.

49 N. G. Saykar, R. K. Pilania, I. Banerjee and S. K. Mahapatra, Synthesis of $NiO–Co_3O_4$ nanosheet and its temperature-dependent supercapacitive behavior, *J. Phys. D: Appl. Phys.*, 2018, **51**(47), 475501.

50 X. W. Wang, D. L. Zheng, P. Z. Yang, X. E. Wang, Q. Q. Zhu, P. F. Ma and L. Y. Sun, Preparation and electrochemical properties of $NiO-Co_3O_4$ composite as electrode materials for supercapacitors, *Chem. Phys. Lett.*, 2017, **667**, 260–266.

51 R. Kumar, R. Thangappan, F. Ran, S. Sambasivam, M. D. Albaqami and S. Mohammad, Enriched performance of practical device assisted asymmetric supercapacitor: NiO/Co_3O_4 intercalated with rGO nanocomposite electrodes, *J. Energy Storage*, 2024, **85**, 111075.

52 J. Wang, L. Ma, W. Tan, S. Wang, J. Wen, Z. Zhang and W. Li, NiO and Co_3O_4 nanoparticles decorated $La_{0.8}Sr_{0.2}MnO_3$-based electrodes for electrochemical NO_x removal in solid electrolyte cells, *Chem. Eng. J.*, 2023, **466**, 143248.

53 A. K. Nayak and H. Han, Surface engineered $NiO–Co_3O_4$ nanostructures as high-performance electrocatalysts for oxygen reduction reaction, *Ceram. Int.*, 2020, **46**(16), 25351–25358.

54 J. Wang, H. Zhang, H. Duan, H. Zhao, J. Qi, B. Ma and H. Fan, Boosting the electrochemical storage properties of Co_3O_4 nanowires by the Mn doping strategy with appropriate Mn doping concentrations, *ACS Omega*, 2024, **9**(6), 6955–6964.

55 A. Behera, D. Seth, M. Agarwal, M. A. Haider and A. J. Bhattacharyya, Exploring Cu-Doped Co_3O_4 Bifunctional Oxygen Electrocatalysts for Aqueous Zn–Air Batteries, *ACS Appl. Mater. Interfaces*, 2024, **16**(14), 17574–17586.

56 G. Yuan, Y. Liu, M. Yue, H. Li, E. Liu, Y. Huang and D. Kong, Cu-doped NiO for aqueous asymmetric electrochemical capacitors, *Ceram. Int.*, 2014, **40**(7), 9101–9105.

57 S. A. A. Shah, N. Gkoulemani, J. T. S. Irvine, M. T. Sajjad and R. T. Baker, Synthesis of high surface area mesoporous $ZnAl_2O_4$ with excellent photocatalytic activity for the photodegradation of Congo Red dye, *J. Catal.*, 2024, **439**, 115769.

58 J. P. Picard, G. Baud, J. P. Besse and R. Chevalier, Croissance cristalline et étude structurale de Co_3O_4, *J. Less-Common Met.*, 1980, **75**(1), 99–104.

59 S. Sasaki, K. Fujino and Y. Takéuchi, X-ray determination of electron-density distributions in oxides, MgO, MnO, CoO, and NiO, and atomic scattering factors of their constituent atoms, *Proc. Jpn. Acad., Ser. B*, 1979, **55**(2), 43–48.

29502 | *J. Mater. Chem. A*, 2025, **13**, 29486–29503

This journal is © The Royal Society of Chemistry 2025

60 H. P. Klug and L. E. Alexander, *X-Ray Diffraction Procedures: for Polycrystalline and Amorphous Materials*, 1974, p. 992).

61 G. A. Begaw, A. K. Worku, D. W. Ayele, T. A. Yemata, T. A. Wubieneh, M. A. Teshager and F. A. Yihun, Enhancing Thermal Properties of Co_3O_4 Nanoparticles Through Optimized Mn-Doping Concentrations, *Int. J. Electrochem.*, 2024, **2024**(1), 7343751.

62 J. Gupta and A. S. Ahmed, Temperature-dependent analysis of dielectric behaviour of Co_3O_4/NiO nanocomposites with varying NiO concentration, *J. Mater. Sci.: Mater. Electron.*, 2022, **33**(31), 24182–24207.

63 S. D. Khairnar and V. S. Shrivastava, Facile synthesis of nickel oxide nanoparticles for the degradation of Methylene blue and Rhodamine B dye: a comparative study, *J. Taibah Univ. Sci.*, 2019, **13**(1), 1108–1118.

64 C. Alex, S. C. Sarma, S. C. Peter and N. S. John, Competing effect of Co^{3+} reducibility and oxygen-deficient defects toward high oxygen evolution activity in Co_3O_4 systems in alkaline medium, *ACS Appl. Energy Mater.*, 2020, **3**(6), 5439–5447.

65 X. Liu, M. Wang and X. Wu, Tailoring electrochemical performance of Co_3O_4 electrode materials by Mn doping, *Molecules*, 2022, **27**(21), 7344.

66 P. Salunkhe, M. A. AV and D. Kekuda, Investigation on tailoring physical properties of Nickel Oxide thin films grown by dc magnetron sputtering, *Mater. Res. Express*, 2020, **7**(1), 016427.

67 B. Laïk, M. Richet, N. Emery, S. Bach, L. Perrière, Y. Cotrebil and P. Dubot, XPS Investigation of Co–Ni Oxidized Compounds Surface Using Peak-On-Satellite Ratio. Application to $Co_{20}Ni_{80}$ Passive Layer Structure and Composition, *ACS Omega*, 2024, **9**(39), 40707–40722.

68 X. Li, W. Kong, X. Qin, F. Qu and L. Lu, Self-powered cathodic photoelectrochemical aptasensor based on in situ–synthesized CuO–Cu_2O nanowire array for detecting prostate-specific antigen, *Microchim. Acta*, 2020, **187**, 1–9.

69 J. Wang, D. N. Mueller and E. J. Crumlin, Recommended strategies for quantifying oxygen vacancies with X-ray photoelectron spectroscopy, *J. Eur. Ceram. Soc.*, 2024, 116709.

70 X. F. Liu, Y. Sun and R. H. Yu, Role of oxygen vacancies in tuning magnetic properties of Co-doped SnO2 insulating films, *J. Appl. Phys.*, 2007, **101**, 123907.

71 S. Oswald and W. X. P. S. Brückner, XPS depth profile analysis of non-stoichiometric NiO films, *Surface and Interface Analysis*, 2004, **36**(1), 17–22.

72 L. Xue, C. Yuan, S. Wu, Z. Huang, Z. Yan, S. Streiff and W. Shen, Preparation of Mn-doped Co_3O_4 catalysts by an eco-friendly solid-state method for catalytic combustion of low-concentration methane, *Catalysts*, 2023, **13**(3), 529.

73 K. Li, D. Xu, K. Liu, H. Ni, F. Shen, T. Chen and H. Lin, Catalytic combustion of lean methane assisted by an electric field over Mn_xCo_y catalysts at low temperature, *J. Phys. Chem. C.*, 2019, **123**(16), 10377–10388.

74 M. A. Peck and M. A. Langell, Comparison of nanoscaled and bulk NiO structural and environmental characteristics by XRD, XAFS, and XPS, *Chem. Mater.*, 2012, **24**(23), 4483–4490.

75 J. Wang, H. Zhang, H. Duan, H. Zhao, J. Qi, B. Ma and H. Fan, Boosting the electrochemical storage properties of Co_3O_4 nanowires by the Mn doping strategy with appropriate Mn doping concentrations, *ACS Omega*, 2024, **9**(6), 6955–6964.

76 A. Sultan, M. Gogacz, J. Lach, R. T. Baker, M. A. Khalid, Y. Ling and K. Zheng, Investigation of Transition Metal-Doped $BaCe_{0.8}Y_{0.2}O_{3-\delta}$ Cathodes for Protonic Ceramic Fuel Cells: Microstructural and Electrical Properties, *Electrochim. Acta*, 2025, 146127.

77 J. Chen, D. Zhang, Y. He, L. Zhang and S. Wang, Enhanced electrochemical performance of SOFC: GDC electrolyte grains encapsulation *via* DZSB film, *Ceram. Int.*, 2024, **50**(3), 5169–5178.

78 M. Dudek, B. Lis, R. Kluczowski, M. Krauz, M. Ziąbka, M. Gajek and A. Raźniak, NiO–$Ba_{0.95}Ca_{0.05}Ce_{0.9}Y_{0.1}O_{3-\delta}$ as a Modified Anode Material Fabricated by the Tape Casting Method, *Materials*, 2022, **15**(7), 2489.

79 S. U. Rehman, M. H. Hassan, S. Y. Batool, H. S. Kim, R. H. Song, T. H. Lim and S. B. Lee, A highly stable Co_3O_4-GDC nanocomposite cathode for intermediate temperature solid oxide fuel cells, *Int. J. Hydrogen Energy*, 2024, **51**, 1242–1254.

80 Y. Wan, Y. Xing, Z. Xu, S. Xue, S. Zhang and C. Xia, A-site bismuth doping, a new strategy to improve the electrocatalytic performances of lanthanum chromate anodes for solid oxide fuel cells, *Appl. Catal., B*, 2020, **269**, 118809.

81 X. Luo, Y. Yang, Y. Yang, D. Tian, X. Lu, Y. Chen and B. Lin, Reduced-temperature redox-stable LSM as a novel symmetrical electrode material for SOFCs, *Electrochim. Acta*, 2018, **260**, 121–128.

82 J. C. Ruiz-Morales, J. Canales-Vázquez, J. Peña-Martínez, D. M. López and P. Núñez, On the simultaneous use of $La_{0.75}Sr_{0.25}Cr_{0.5}Mn_{0.5}O_{3-\delta}$ as both anode and cathode material with improved microstructure in solid oxide fuel cells, *Electrochim. Acta*, 2006, **52**(1), 278–284.

83 C. Solís, L. Navarrete, F. Bozza, N. Bonanos and J. M. Serra, Catalytic surface promotion of composite cathodes in protonic ceramic fuel cells, *ChemElectroChem*, 2015, **2**(8), 1106–1110.

84 Z. Xu, Y. Li, Y. Wan, S. Zhang and C. Xia, Nickel enriched Ruddlesden-Popper type lanthanum strontium manganite as electrode for symmetrical solid oxide fuel cell, *J. Power Sources*, 2019, **425**, 153–161.

85 Q. Wang, Z. Hu, L. Xu, J. Li, Q. Gan, X. Du and M. Ouyang, A comparative study of equivalent circuit model and distribution of relaxation times for fuel cell impedance diagnosis, *Int. J. Energy Res.*, 2021, **45**(11), 15948–15961.

86 J. Zhang, L. Lei, H. Li, F. Chen and M. Han, A practical approach for identifying various polarization behaviors of redox-stable electrodes in symmetrical solid oxide fuel cells, *Electrochim. Acta*, 2021, **384**, 138340.

This journal is © The Royal Society of Chemistry 2025

J. Mater. Chem. A, 2025, **13**, 29486–29503 | **29503**